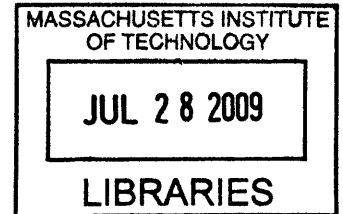# Atomistic Calculations of Rate of Long-timescale Microstructural Evolution

by

Timothy Tin-Ming Lau

B.S. Materials Science and Engineering
Cornell University, 2005

SUBMITTED TO
THE DEPARTMENT OF MATERIALS SCIENCE AND ENGINEERING
IN PARTIAL FULFILLMENT OF THE REQUIREMENTS FOR THE DEGREE OF

DOCTOR OF SCIENCE IN
MATERIALS SCIENCE AND ENGINEERING
AT THE
MASSACHUSETTS INSTITUTE OF TECHNOLOGY

JUNE 2009

Signature of Author: _____
Department of Materials Science and Engineering
May 1, 2009

Certified by: _____
Sidney Yip
Professor of Nuclear Science and Engineering
Professor of Materials Science and Engineering

Accepted by: _____
Christine Ortiz
Professor of Materials Science and Engineering
Chair, Departmental Committee on Graduate Students

Atomistic Calculations of Rate of Long-timescale Microstructural Evolution

by
Timothy Tin-Ming Lau

Submitted to the Department of Materials Science and Engineering
on May 1, 2009, in partial fulfillment of the
requirements for the degree of
Doctor of Science in Materials Science and Engineering

Abstract

The ability to investigate materials systems at the resolution of individual atoms makes computational simulations a powerful tool for the study of materials phenomena. However, microstructural evolution in complex materials is only meaningfully characterized in laboratory or industry applications by deformation rate and relevant rate coefficients, quantities that require sampling over a timescale too large for traditional atomistic methods to probe. New methods and techniques have to be developed in order to obtain useful information of rate from atomistic simulations. In this thesis, we explore a set of four problems, related to two long-timescale microstructual phenomena, creep and oxidation, and use a variety of atomistic methods appropriate to each problem to demonstrate the techniques of obtaining rate information.

Creep due to vacancy-driven dislocation climb critically depends on the movement of the vacancies in the bulk towards dislocation cores, and for the first contribution of the thesis we investigate the influence of carbon solute atoms on vacancy diffusion pathways in bulk BCC Fe. Using these results, we draw explanations of the trends of the experimentally-observed rate of creep.

It is well-known that vacancy energetics vary with distance from dislocation cores due to the dislocation strain field, but the effect this has on creep by the dislocation climb mechanism is not well understood. In the second contribution of the thesis, we present an investigation of the vacancy-dislocation interaction of BCC Fe. By obtaining the details of the unit processes of vacancy migration around a dislocation core and formulating this information appropriately for numerical techniques based on transition-state theory, we enable the calculation of the dislocation climb rate with full atomistic detail.

In the oxidation of metals, the transport of cations through the surface oxide film governs the overall material degradation. In the third contribution of the thesis, we present calculations of the energetics of defect formation and migration in nonstoichiometric $Fe_{3-\delta}O_4$ spinel, which is closely related to the oxide film on Fe. We

provide an explanation of experimental integral measurements of diffusion rate in a mechanistic, unit-process way.

Creep of nanocrystalline materials is a new area of interest as fabrication techniques begin to impinge on this lengthscale; nonetheless, this phenomenon is not well understood and existing computational studies all involve unrealistic thermal or mechanical loading conditions. In the last contribution of the thesis, we present an investigation of the creep of Fe nanocrystals, employing a novel method of activating states to directly calculate a rate. We reach a rate regime that is inaccessible by traditional methods as well as identify some of the relevant unit processes in this type of creep.

The rates of these slow dynamics phenomena are all investigated on the basis of their atomistic unit processes. However, there are differences in how information of the unit processes is obtained from atomistic calculations and in how the properties of these unit processes are subsequently used to understand the overall rate. That different investigation approaches are needed is a direct result of the variation in the complexity of the microstructures, the number and predictability of atomic transition mechanisms, and the depth of existing experimental knowledge. These four studies therefore represent distinct, but complementary, challenges within the common theme of rate calculation. We conclude the thesis with an appraisal of the types of challenges encountered and with an evaluation of the approaches we took to the problems.

Thesis Supervisor: Sidney Yip
Titles: Professor of Nuclear Science and Engineering,
Professor of Materials Science and Engineering

Acknowledgements

The success of the studies outlined within this thesis would not have been possible without the help of my scientific collaborators. I would like to thank these individuals:

- Dr. Clemens Först, for helping me understand how to perform *ab initio* calculations and learn the basic ideas of atomistic simulations

- Professor Julian Gale of the Curtin University of Technology, for modifying his GULP code [1] to enable me to use it to fit the potential described in Chapter 3

- Dr. Mukul Kabir, for performing the energy barrier calculations described in Chapter 3, and for implementing the kinetic Monte Carlo scheme described in the end of Chapter 4

- Mr. Paul Monastario, for pushing the study in H effect on the Fe-C system far beyond where I left it off

- Professor Xi Lin of Boston University, for helping me understand some of the subtle physics involved in periodic systems and in extended defects

- Professor Rüdiger Dieckmann of Cornell University, for the extremely helpful discussions on the subtleties of the highly complex magnetite oxide

- Dr. Akihiro Kushima, the developer of the autonomous basin climbing method, for his help in adapting his original code to study Fe nanocrystals and for helpful discussions on calculating rate

- Professor Krystyn Van Vliet, for helpful discussions on the studies outlined in Chapters 3 and 4

- My thesis committee members, Professor Bernhardt Wuensch and Professor Samuel Allen, for their valuable comments on this thesis text and for encouraging me to seek the connections between the four contributions in this thesis

Most of all, I cannot overstate the importance of my advisor Professor Sidney Yip to the success of this thesis. He has played a role in everything big and small, from the minor grammatical corrections to the concept of calculating rate from atomistic methods itself. I do not think it is possible to separate out and identify his contributions to the thesis, as his influence is evident on every single page. The very existence of the thesis document itself is testament to the assistance he has rendered me and my intellectual development and growth under his guidance over the last four years.

I would be remiss if I did not acknowledge the indirect contribution made by my family. To them, eternal thanks for being my greatest and most persistent supporters.

MIT has been my home for the last 4 years. The experience arguably began with my application essay, which I started off with the words of Vergil, *"felix qui potuit rerum cognoscere causas"* (*Georgics*, 2.490). (The alert reader can recall this line inscribed over the east entrance of Building 6.) As I complete the journey by writing these last words of my thesis, it is only appropriate, for the sake of symmetry, that I conclude with another immortal line of the master,

"forsan et haec olim meminisse iuvabit" (*Aeneid*, 1.203)

Contents

List of Figures

List of Tables

1 Introduction

1.1 Slow Dynamics

In a 2002 review paper on creep at very low rates [2], F.R.N. Nabarro summarizes the challenge to, as well as the possible contribution of, the atomistic computational modeler in the understanding of long-timescale evolution of microstructure in materials with industrial relevance,

> A land-based turbine may have a life of 40 years. If a total creep strain of 1 pct is permissible, the creep rate is about 10^{-11} s^{-1}. Extrapolation to this rate from rates measureable in the laboratory is perilous, and we need to understand the physical processes involved .... The present state of knowledge reveals specific questions that call for experimental investigation. Theory will contribute, but atomistic computation, with a time scale of 10^{-11} s, will not handle processes that take 10^{11} s. Computation on the dislocation scale may perhaps become helpful in a few years time.

In terms of the traditional atomistic method of molecular dynamics [3], it is easy to understand the pessimism of Nabarro. Even with all sorts of creativity in getting the best out of the method, like those implemented in state-of-the-art multimillion-atom simulations (see [4] for an example), molecular dynamics (MD) itself is still fundamentally constrained by the need of accurate numerical integration of the equations of motion in computational timesteps of 1 fs to 10 fs. Even if humanity ever develops the necessary computer machinery for the task, it will never be practical, from the point of

view of analyzing data and obtaining understanding, to meet Nabarro's challenge of simulating 10^{11} s phenomena by breaking the simulated time into 10^{26} discrete units.

Thus these problems of slow dynamics in complex materials, which could not be directly simulated using MD, require an alternate approach. The key to doing this is to first understand why these problems are long timescale in nature. Transition-state theory [5] informs us that the rate of an atomistic transition has an $\exp\left(-\Delta E / k_B T\right)$ dependence on the activation barrier ΔE. As such, in the presence of a significant energy barrier to kinetic transitions (on the order of 1 eV), real material systems (and MD model systems) spend the bulk of the time trapped in deep energy minima, with transitions between energy minima over energy saddle points being rare events. Microstructural evolution is simply the aggregate result of many such rare transitions and MD cannot be used to sample enough of these transitions to simulate the general phenomenon. However, rather than directly tracking the exact trajectory of the atomic system, as is done in MD, the long-timescale microstructure evolution can be modeled by abstraction into unit processes of transitions between minimum energy states, each with an associated deformation unit and time unit. Such a concept is not new and has been used with success in analytical treatment of simple vacancy and interstitial diffusion problems [6]. The challenge lies in directing the computation effort to investigate the transitions and in incorporating the atomistic details within the basic framework to extend its use into more complicated materials problems. In this thesis, we will use this type of approach to investigate topics relevant to the slow dynamics phenomena of creep* and of oxidation†.

---

* Creep is the inelastic deformation of materials that occurs, due to microstructural processes, over time as the material is subjected to continuous applied mechanical loading.
† The equilibrium state of the typical metal (in its pure, elemental form) in contact with oxygen is some form of oxide. The process of metal oxidation is the growth of the oxide film on the surface of the metal.

The first of such problems that we investigate is the point defect population and interactions in high carbon ferritic steels*. These metastable materials are supersaturated with both extrinsic (carbon, ~ 4 at. %) and intrinsic (vacancy, ~ 0.5 at. %) defects in the body-centered cubic (BCC) Fe matrix. The tendencies of point defects to form complex point defect clusters in this material [8] can have important consequences on the diffusive behavior and in turn have an effect on the material deformation, as the alloy is known to creep by vacancy-driven dislocation climb [9]. In this creep mechanism [10], sustained deformation requires a steady transport of vacancies to the dislocation cores in order to permit dislocations trapped at obstacles on their glide planes to climb onto another plane for continual movement. We can therefore build up an understanding of the creep deformation rate of the material by studying the formation of the point defect clusters and their effect on diffusion rates.

We also consider how vacancies behave in the stress fields of the dislocation, how they bind with the dislocation itself, and how they contribute to the dynamic structure of the dislocation. Even though some account of these vacancy properties is necessary in any treatment of the dislocation climb rate, the study of these atomistic details is neglected, due in no small part to the great complexity in making use of the results in analytical equations, the traditional choice of theoretical approach to dislocation climb [11, 12]. However, with the availability of numerical methods now capable of handling these details, such as atomistic techniques based on transition-state theory like kinetic Monte Carlo (kMC) or continuum transport equation-solving methods like the finite-element method (FEM), investigating the properties of the vacancy in relation to a

---

* Iron in its low-temperature, ferromagnetic, body-centered cubic (BCC) form is known interchangeably as ferrite or α-Fe. This is the stable form of pure Fe below 1184 K and has a solubility limit with relation to the carbon content of about 0.1 at. %. Details of the Fe-C binary system can be found in [7]. It must be noted that the word "ferrite" can also refer to the general class of spinel oxides of the form AB_2O_4. To avoid confusion, within this thesis the noun "ferrite" and the adjective "ferritic" will only be used to refer to BCC Fe.

dislocation can greatly benefit the modeling of the dislocation climb and understanding of this important creep mechanism.

For the third component study of the thesis, we examine the cation diffusion in magnetite Fe_3O_4, which is closely related to the oxide layer on Fe [13]. The transport of cations through the oxide layer on a metal is necessary to continue the reaction of the metal atoms with oxygen molecules from the environment to form oxide [14]. Our study into the diffusion properties in the oxide can therefore help build the understanding of the rate of metal oxidation.

Finally, we investigate the atomic motion at and near the highly irregular grain boundaries of nanocrystalline materials and correlate them to the rate of deformation which we directly calculate. Understanding the relationship of such processes to the rate of creep deformation is of great importance. The grain boundaries are the dominant component of the microstructure in the length scale of these materials. The creep mechanisms responsible for the deformation of materials with larger grains that involve dislocations are thus suppressed [15]. Existing atomistic work in this area conducted with MD have all utilized either extreme stress [16] or extreme temperatures [17] in order to overcome the limitation of the method in dealing with slow deformation. While these studies yield reasonable trends and some useful conclusions, they all provide unrealistic strain rates and fail to produce convincing unit mechanisms responsible for the deformation. We aim to provide this missing understanding of the creep phenomenon by using a new approach to simultaneously obtain realistic strain rates and atomic unit processes.

1.2   Scope of Thesis

In this thesis, we explore four problems relevant to the long-timescale phenomena of creep and metal oxidation. In Chapter 3, we examine the point defect interactions and their contribution to diffusivity in BCC iron supersaturated with carbon and vacancies. We begin with the construction of an empirical energy model relevant to the system. We use the formation energetics of the various defect types to obtain the defect population and we investigate the activation energies of the defect migration mechanisms. We combine these results to analytically obtain the diffusive behavior in the material, with which we obtain possible explanations for the experimentally-observed rate of creep in the material that arises from dislocation climb [9].

In Chapter 4, we discuss another aspect of dislocation climb, namely, the behavior of vacancy diffusion near the core. We show how vacancy-dislocation interaction energetics at the core deviate from elasticity predictions [18] and how the vacancy diffusion barriers vary with distance from the core. We also demonstrate that the vacancy interaction with the dislocation core can be compared to a particle adsorption problem. We illustrate how these vacancy properties, when formulated as deviations from the bulk crystal behavior, can be tractably transferred into numerical simulations of climb. We close with a description of a kMC scheme to numerically calculate the dislocation climb rate and material creep rate using our calculated atomistic details.

In Chapter 5, we present a study, associated with the problem of oxidation, of the cation diffusion in nonstoichiometric magnetite $Fe_{3-\delta}O_4$, a related structure of the spinel oxide film on Fe metal surface [13]. We calculate the defect energetics as well as the activation energies of the defect transport mechanisms. We use our results to interpret experimental measurements of the integral properties of nonstoichiometry and

diffusivities [19, 20] in a mechanism-specific way, and create a combined experimental and computational understanding of the defect population and transport rate in the spinel.

In Chapter 6, we present an investigation on creep in nanocrystalline Fe. We employ a novel method of activated kinetics, successful in explaining shear relaxation over a wide range of temperatures in supercooled liquids, to directly calculate a strain rate of solid-state deformation under stress. We identify the relevant grain-boundary unit processes and explain their contribution to the overall material deformation.

As discussed in Section 1.1, we attack the general issue of slow dynamics with the general scheme of breaking down the investigated phenomena of microstructural evolution into its component transitions and obtaining the rate from the properties of these unit processes. However, the four problems investigated differ in the chemistry, in the levels of system symmetry, and in the state of experimental knowledge, and so require different approaches to calculate and understand rate. They are therefore complementary in that they highlight the wide range of challenges in the calculation of rate. In Chapter 7, we discuss these issues, along with possible future developments in the area.

2   Coarse-Graining the Energy Landscape

2.1   The Energy Landscape Concept

Using the Born-Oppenheimer approximation, the energy of an atomic system could be approximated as a function strictly of the atomic coordinates $\vec{R}$ of the N atoms in the system. This energy function $\Phi(\vec{R})$ is a complicated hypersurface, or landscape, of 3N dimensions, as there are 3 degrees of freedom for the position of each atom. As an atomic system evolves and runs through different possible atomic configurations, it traces a line through the energy landscape.
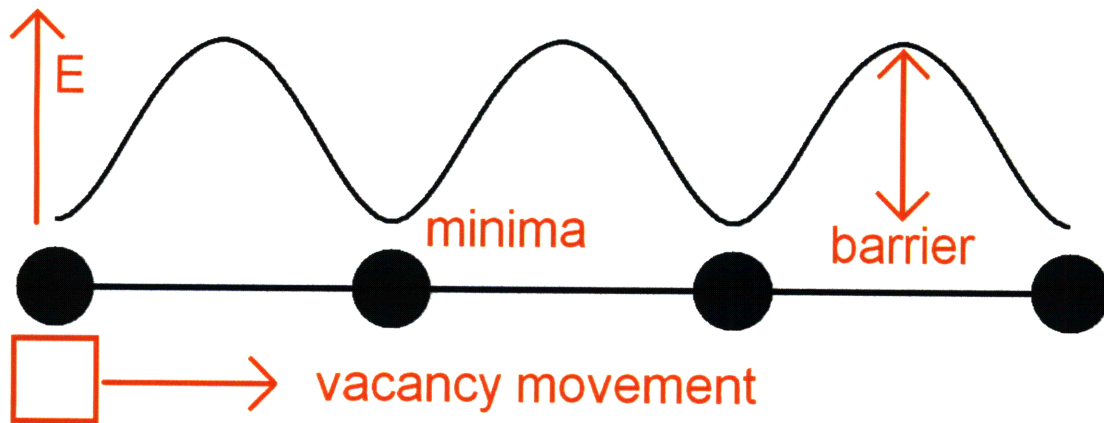
Figure 2-1: A schematic of the energy landscape for a vacancy diffusion problem in a one dimensional atomic lattice.

There are 2 particularly important topological features on the energy landscape. Figure 2-1 illustrates the principle for the simple case of a vacancy moving in a 1 dimensional lattice. The energy minima correspond to stable or metastable states, which are typically given qualitative labels (in Figure 2-1, a vacancy at "rest" at some arbitrary lattice position). The saddle points correspond to the transitions between minima [5] (in Figure 2-1, the jump of a vacancy from an arbitrary lattice position to a nearest neighbor

position). The height of the saddle point ΔE corresponds to the kinetic barrier and governs the rate of the corresponding transition

$$\Gamma = \nu_{\circ} \exp\left(-\frac{\Delta E}{k_B T}\right)$$

A theoretical derivation of this so-called Arrhenius dependence as well as the meaning of the prefactor $\nu_{\circ}$ could be found in [5]. By nature of the exponential dependence, transitions are fundamentally rare events if the barrier heights are significant (i.e. on the order of 1 eV), as is in the cases of creep and oxidation. As a result, materials systems spend the bulk of the time trapped in deep energy minima and microstructural evolution is therefore long timescale in nature.

In the thesis, we coarse-grain the energy landscape out to only the energy minima and saddle points, in accordance with the principles of transition-state theory [21]. We associate each minimum with an average time the system spends within it between transitions, and by comparing the extent of deformation between each minimum we can obtain a rate of deformation. While we give up tracking explicitly the evolution of atomic positions as is done in traditional molecular dynamics, we can direct the computation effort specifically at searching for transitions and calculating rate and avoid spending the resources calculating the trajectory of the atoms as the system hovers around deep energy minima.

2.2 *Ab Initio* and Empirical Energy Models

The choice of the energy landscape in an atomistic simulation is of crucial importance. Care must be taken to weigh accuracy (in terms of simulating well the properties of the material) versus computational expense. In this thesis, we use two types of energy model: density functional theory (DFT), a type of *ab initio* energy model, and Finnis-Sinclair (FS), a type of empirical multibody potential.

Density functional theory (DFT) belongs to the class of electronic structure methods, where energies are obtained from solving Schrödinger's equation for atomic systems. While DFT is a relatively recent development, it is by now a well-established formulation. Details about the method can be found in texts [22]. It is a very versatile and powerful tool that can deliver reliable results, and as an *ab initio* model it requires no input save the atomic configuration. Its main disadvantage is that it is extremely expensive to use computationally*, and, with the current equipment of research-group scale, calculations could not be done on systems of more than 500 atoms. In terms of this thesis, this limitation means that the method is suitable only for the investigations involving lattice point defects detailed in Chapter 3 and Chapter 5, and even then restricted to energy minimization or selected nudged elastic band (NEB) problems. Whenever mentioned in this thesis, it is always used as implemented in the VASP package [24]. Further details about the calculation methodology can be found in [25].

The Finnis-Sinclair (FS) model [26] is a variant of the embedded-atom model [27] type of empirical potential. Potentials of this type have been particularly successful in

---

* DFT is a method whose demand on computational resources (e.g. memory, computational time) scales to N^3, where N is the number of electrons in the system. Each of the N electron wavefuntions must be kept orthogonal to obey the Fermion statistics. Because of the delocalized nature of electron wavefuntions, these N^2 integration must be conducted over the entire simulation cell, which scales with N [23]. This nonlinear scaling makes calculations involving many electrons impractical to perform.

modeling transition-metals and alloys. In the FS model[*], the energy of each atom in the system is written as

$$E_{\alpha,i} = -A_\alpha \sqrt{\sum_{j \neq i} \rho_{\beta\alpha}\left(r_{ij}\right)} + \frac{1}{2}\sum_{j \neq i} \phi_{\beta\alpha}\left(r_{ij}\right)$$

where j refers to the nearest neighbors within a cutoff distance, α is the element type of atom i, β is the element type of atom j, A_α is a positive coefficient specific to element α, r_{ij} refers to the interatomic distance between atoms i and j, $\rho_{\beta\alpha}\left(r_{ij}\right)$ refers to the density contribution[†] of j to atom i, and $\phi_{\beta\alpha}\left(r_{ij}\right)$ refers to the pair interaction between atoms i and j. An attempt at justifying the form of the potential can be found in [29]. This type of energy model is significantly cheaper computationally than DFT[‡] to use in atomistic simulations and could be used for exploring large systems or for sampling large numbers of transitions. In this thesis, the construction of a potential of this form for the Fe-C alloy system is discussed in Chapter 3, and the use of the potential can be seen in the investigations detailed in Chapters 3, 4, and 6.

---

[*] The original Finnis-Sinclair model [26] does not provide for a multi-element formulation. The extension of the basic form for use in duplicating alloy energetics is a later development; a discussion can be found in [28].

[†] The sum of the density contributions is essentially a measure of coordination.

[‡] Empirical potentials generally treat atomic interactions in a highly localized manner. For instance, in the Fe-C potential discussed in Chapter 3, the Fe-Fe interaction is limited to the interactions between 1st and 2rd nearest neighbors. As a result, the computational intensity scales to the number of atoms N instead of N^3 as in DFT.

2.3 Energy Landscape Exploration

Our approach to calculating rate lies in coarse-graining the energy landscape into the most essential features of the energy minima and energy saddle points. How we search for these topological features is thus extremely important. We will here briefly describe the techniques for doing so.

2.3.1 Energy Minima

As mentioned in Section 2.1, the energy minima of a system are typically of great importance to the atomistic modeler. However, due to the complexity and the large dimensionality of the energy landscapes, one typically cannot locate minima by analytically solving for zeroes in the derivatives of the energies (with respect to atomic positions). Well-established mathematical techniques have been developed, however, to overcome this difficulty by tracing a downward path along the energy landscape surface to a local minimum from an initial starting guess. A class of methods involves finding the path using the local gradient[*]. Such methods include quenched molecular dynamics and conjugate gradients [30]. More refined methods include using the local Hessian of second derivatives[†], such as the rational function optimization [31] method, or an estimate of the local Hessian, such as the Broyden, Fletcher, Goldfarb, and Shanno (BFGS) method [32], to assist in the search.

---

[*] The gradient of a function marks the direction in which the function changes most rapidly. The methods described all use the general principle, with adjustments for computational efficiency, of following the direction of the negative gradient to reach local minima.

[†] The Hessian of a function describes its local curvature. As the Hessian contains more local information of the function than the gradient, it is used in cases where more refined minima searches are needed. It should be noted that the gradient of a N dimensional function has N components, while the Hessian matrix has N^2 components. The computational demand (e.g. memory) for the use of Hessian scales appropriately.

In this thesis, all of the above mentioned methods have been used for energy minima search when and where appropriate. As these techniques do not yield different results, we will typically not specify the algorithm used. A general discussion of this subject area can be found in [33].

2.3.2   Energy Saddle Points

There exists a variety of search methods for energy saddle points; in this section we will describe the two techniques that are used in this thesis.

The nudged elastic band (NEB) method is a relatively recent development that has become quite well established within the atomistic simulations community. The details of the method can be found elsewhere [34] and we will here summarize only the most essential ideas.

The general class of "chain-of-states" methods has at its core the concept of representing a transition by certain discrete, but sequential, images of the atomic positions interconnected via fictional springs along its path on the energy landscape. NEB is a numerical variant that quite efficiently converges upon the minimum energy path, which then yields the energy saddle point through the energy value that represent the local maximum along the path.

In the NEB method, one starts with an initial guess of images along a path between two minima, typically by linearly interpolating at regular intervals between the minima. During each calculation cycle, each image i is permitted to evolve with the force

$$\vec{F}_i = -\vec{\nabla}\Phi\left(\vec{R}_i\right)\Big|_{\perp} + \vec{F}_i^{\,s} \cdot \hat{\tau}_{\parallel}\hat{\tau}_{\parallel}$$

The first term in the sum is the component of the Newtonian force $\vec{\nabla}\Phi\left(\vec{R}_i\right)$ on the image that is perpendicular to the path, obtained from the energy landscape $\Phi\left(\vec{R}_i\right)$. The Newtonian force drives the image towards energy minimization, and using strictly the component of that force that is perpendicular to the path allows the energy to minimize towards the path and not slide down to the minimum. The second term in the sum is the force of the springs connecting an image with its preceding and following images

$$\vec{F}_i^s = k\left(\vec{R}_{i+1}-\vec{R}_i\right) - k\left(\vec{R}_i-\vec{R}_{i-1}\right)$$

projected along the unit tangent to the path $\hat{\tau}_{\parallel}$. The spring force guarantees that each of the images during the calculation cycle remains connected with one other, in order, by shortening the distance between images. Utilizing only the component of this force in the direction of the path removes the shortening tendency of the spring force to pull images off curvilinear minimum energy paths. This process is iterated until convergence is reached.

There are many improvements to the method, such as manipulating the image with the highest energy to converge onto the saddle point [35] or better estimates of the unit tangent to the path $\hat{\tau}_{\parallel}$ [36], but all stay within the basic framework.

The method is the primary tool in the investigations detailed in Chapters 3, 4, and 5, as the atomistic transitions in these problems have relatively identifiable initial and final states.

The other method of saddle point search that we utilize is the autonomous basin climbing (ABC) method [37]. The method operates by a series of elementary steps of alternating activation and relaxation, which allows a system to climb up an arbitrary energy potential well. On the energy landscape where there are many local minima and

saddle points, having the ability to climb out of any potential well means that one can then sample the topography by generating an explicit trajectory for the transition-state pathway. The system evolution, on an energy scale, is therefore described by this trajectory. As the method is very recent, we will here detail its basic operation as well as provide an example of its use.

Figure 2-2(a) shows the two elementary steps of activation and relaxation that move the system up a particular potential well. The procedure begins with an energy minimized configuration, where an activation step is created by adding a 3N dimensional Gaussian penalty function (N is the number of atoms in the system) to the initial coordinates $\vec{R}_{\circ}$

$$\phi(\vec{R}) = W \exp\left[\frac{(\vec{R} - \vec{R}_{\circ})^2}{2\sigma^2}\right]$$

where W (with units of energy) and σ (with units of distance) determine the strength and spatial extent of the penalty respectively. These parameters must be determined for the specific situation for which the method is used. The penalty is added to the local energy to obtain a total system energy Φ'

$$\Phi' = \Phi(\vec{R}) + \phi(\vec{R})$$

The added penalty has the effect that, upon minimization of the combined energy (sum of the penalty and the original potential energy of the system) with relation to the atomic coordinates, the system is pushed away from the initial minimized configuration into a higher energy state. A new penalty is then added and the cycle of minimization and penalty addition is begun anew. With sufficient energy penalties accumulated after a series of such steps, the system will cross an energy saddle point during a relaxation step and enter into an adjacent well. Starting at the bottom of this well the activation-relaxation series is repeated until the system is able to escape from the second well.

30

Notice that the energy penalty functions imposed in the previous activation steps are not removed during the entire sampling, so that the system is always discouraged from returning to previously visited potential minima. Thus with this method one is not sampling a fixed energy landscape, rather one that evolves along with the sampling such that the system is always encouraged to sample new regions. This method, in contrast to saddle point sampling techniques such as NEB, does not require *a priori* knowledge of the final state. This is particularly useful for the system where the structure is too complex to generate such an input.
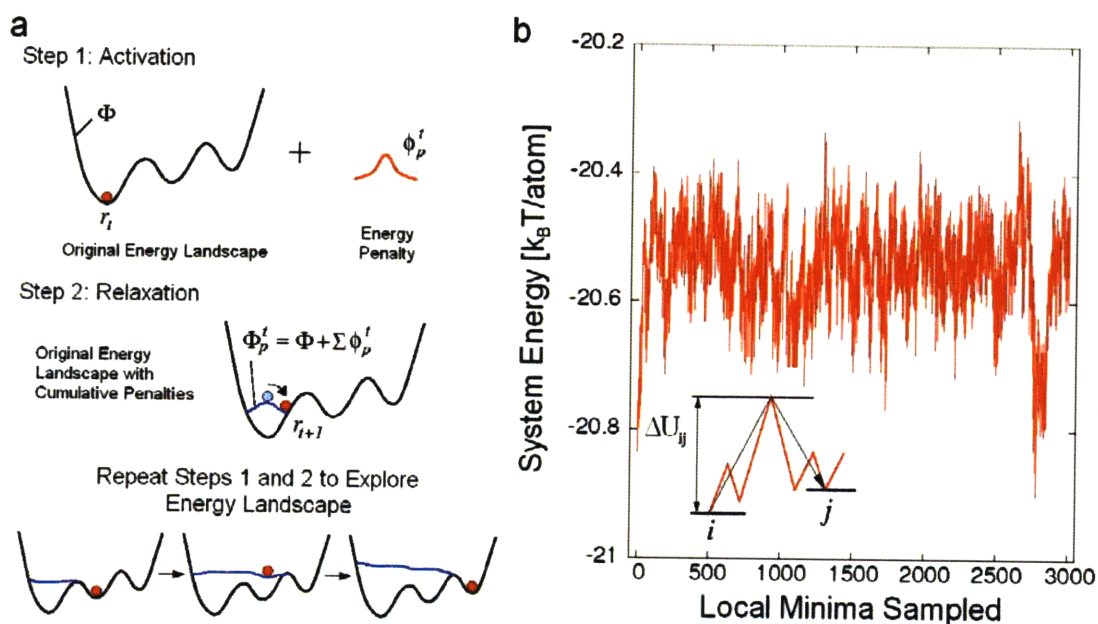
Figure 2-2: The autonomous basin climbing (ABC) technique. (a) A schematic representation of the method – an energy minimized initial structure is activated by imposing on the energy landscape Φ a Gaussian energy penalty ϕ_p^t (centered at the original configuration), which causes the system to climb up the basin into a higher energy configuration. Repeated application of the energy penalties will eventually cause the system to move to another energy minimum. (b) An illustration of the results obtained from ABC, where a series of interconnected energy minima and saddle point transitions between them is obtained. Activation barrier between two minima i and j, ΔU_{ij}, is defined by the saddle energy between the two as shown in the inset.

31

This method has been used to obtain transition-state pathway trajectories in supercooled liquids. An example is shown in Figure 2-2(b). The trajectory is an alternating sequence of energy minima and saddle points that allow the system to evolve along a particular energy pathway. From such data we can extract an effective temperature-dependent activation barrier, shown in the inset in Figure 2-3, which in turn determines the temperature variation of the shear viscosity through the application of transition-state theory [37]. Figure 2-3 shows that the atomistic results for amorphous SiO$_2$ [38] and a model of binary Lennard-Jones interaction [39] have the same behavior as existing experimental viscosity data [40]. We regard this agreement as a sign of promise that the method is capable of probing the rate of microstructural evolution of materials over a wide temperature and temporal range.

The method is the primary tool in the investigation of creep in nanocrystalline Fe detailed in Chapter 6. The main reason for its use lies in the microstructure of interest, which consists of a large volume fraction of grain boundaries where the most important atomistic transitions are expected to take place. Due to the complicated disordered structure, plausible transitions from any initial configuration are too numerous to investigate individually by NEB, even if the problem of identifying the end states of these transitions is surmounted. In addition, the characteristics of the atomic transitions that occur are expected to differ as the microstructure of the grain boundary evolves due to the external driving force (i.e. stress). That ABC does not require guesses of the final states and that it can provide a trajectory of the system deformation renders it an ideal choice for investigating this problem.
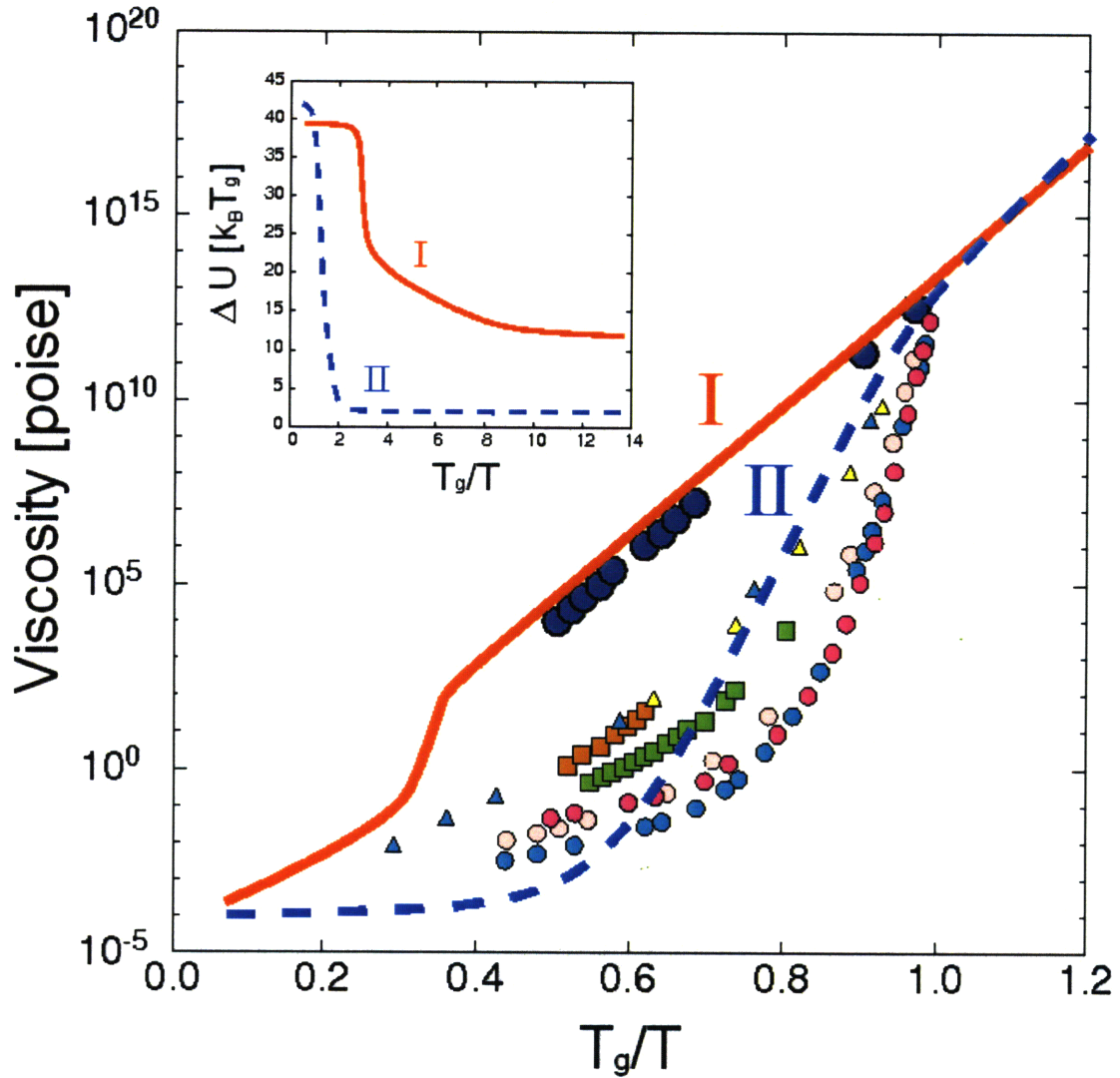
Figure 2-3: The viscosity of supercooled liquids as calculated using the ABC method (solid and dashed curves) [37] in comparison with experimental measurements (symbols [40]). I and II denote amorphous SiO_2 [38] and binary Lennard-Jones model [39], respectively. The inset shows the extracted activation barriers as a function of temperature. T_g is the glass transition temperature where the viscosity is 10^{13} poise.

3   Vacancy and Solute Interaction in Fe Supersaturated with Carbon Solute

3.1   Experimental Background

Steels with a high carbon concentration beyond the eutectoid point at 0.77 wt.% have since historical times been utilized, such as in the case of "Damascus steel" scimitars, for their impressive mechanical properties, particularly, toughness [41]. These steels are used in a state far out of equilibrium, with a supersaturation of carbon atoms in the ferritic BCC matrix and with the Fe_3C cementite fraction kept low compared to the equilibrium state. It is this complex microstructure which results from its thermodynamic metastability that confers superior mechanical properties. Yet these materials are subject to creep failure at high applied stresses σ (normalized by Young's elastic modulus E as $\sigma/E = 10^{-3} - 10^{-2}$). Figure 3-1(a) illustrates this experimental trend, wherein different research groups [42, 43, 9] measured appreciable effective strain rates of ferritic steels, normalized by the effective temperature-dependent self-diffusivity D_{eff} in each experiment, and indicate power-law stress dependences of power n of 5 - 8. This power-law dependence is consistent with vacancy-driven dislocation climb creep [9].
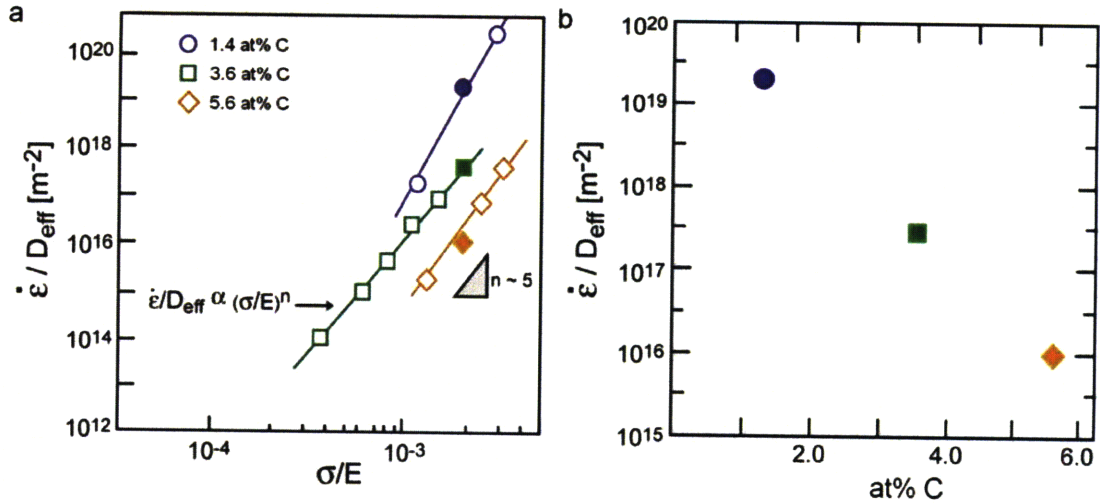
Figure 3-1: Experimental creep strain rates in high-carbon steel. (a) Normalized strain rates $d\varepsilon/dt$ increase strongly with increasing normalized stress σ, where D_{eff} is Fe self-diffusivity and E is elastic modulus. Experiments were conducted at $T/T_m \sim 0.45$, where the creep strain rates were readily measurable. The power-law stress dependence n of 5-8 is a signature of creep by the vacancy-driven dislocation climb mechanism [9]. (b) At a given stress magnitude, creep strain rates decrease with increasing carbon content. Data from [42, 43, 9].

It is difficult to understand these creep trends from experiments alone. As seen in Figure 3-1(b), the aforementioned studies indicate a decreased creep strain rate with increasing total carbon content, contrary to observed trends in the face-centered cubic (FCC) phase[*] (as a function of carbon [44] or palladium [45] solute content) as well as the theoretical understanding that dilute solute atoms generally increase self-diffusivity [46]. As current experimental techniques cannot provide full details of the microstructure (e.g. how carbon solute atoms are distributed throughout the bulk), it is not simple to attribute this discrepancy, based purely on experiment results, to sources such as a differential distribution of the carbon from grain interiors to boundaries or a differential concentration of carbon-vacancy clusters that reduces iron self-diffusivity.

---

[*] The FCC phase is the equilibrium phase of iron from 1184 K to 1665 K, and is known interchangeably as austenite or γ-Fe. Details of the Fe-C binary system can be found in [7].

In this study, we aim to use atomistic simulations to develop an understanding of these trends. We first investigate the migration mechanisms and activation barriers of defect clusters consisting of Fe vacancies and C solute atoms within a model system of BCC Fe bulk, and construct an analytical framework to calculate the diffusion rate incorporating these atomistic details. As the rate of creep by the vacancy-driven dislocation climb mechanism is proportional to the rate of diffusion [10], our calculated trends could be used to understand the experimental creep rate.

3.2   Developing an Appropriate Energy Landscape

As discussed in Section 2.2, an energy model suitable for simulating the microstructure is necessary. We therefore begin our investigation with identifying the essential features we require out of any energy model we use.

3.2.1   Potential Criteria and Benchmarking of Existing Potentials

DFT has been used with success to examine the basic energetics of defect formation in the BCC Fe with a variety of solute atoms (Cu [47], C [8], and N [8]). However, as discussed in Section 2.2, the energy model, although accurate, is very computationally expensive to use. Given the large number of lattice defect clusters and associated migration pathways that have to be sampled in this study, it could not be used for anything more than a reference energy landscape. Empirical potentials are more appropriate for the task and are open for future extensions into calculations involving large systems (e.g. dislocation studies). However, we could not expect that these potentials would be able to duplicate the entire DFT energy landscape of C solute atoms in the BCC Fe matrix. As such, it is necessary to establish a list of the most basic criteria

36

appropriate for the specific problem of studying defect pathways in BCC Fe supersaturated with C:

1. Represent well the basic properties (e.g. elastic properties) of BCC Fe.

2. Accurately account for the key minima of C interstitial atoms (e.g. octahedral interstitials) in BCC Fe.

3. Energetically distinguish multiple, slightly different defect configurations of key defect clusters relevant to BCC Fe supersaturated with up to 10 wt.% C.

The fulfillment of requirements 1 and 2 would allow the potential to compare with what little experimentally available data there is of the BCC Fe lattice and of the basic thermodynamics of embedding carbon solute in Fe. Requirement 3 is important as it is known from DFT calculations that complicated defect clusters consisting of multiple carbon atoms and iron vacancies are expected within the matrix [25]. These defects can take multiple configurations, some of which can be seen in [8]. Being able to replicate the energy of formation of the key energy minima (i.e. the deepest minima) and at least correctly rank, even if not hitting the exact energy targets, the less important energy minima would guarantee that the potential could reproduce the thermodynamics of the defect species and provide the ability to model the defect transport pathways.

Finally, while it is not entirely necessary for the potential to be capable of doing so, there are advantages if it can favor the formation of Fe_3C as an equilibrium phase, which is achieved by a correct representation of the energy of formation of the structure (and to a lesser degree, the exact structure) [48]. This is to ensure that the potential can at least duplicate the Fe-C phase diagram for low temperatures [7] and would accurately reflect a carbon-supersaturated BCC lattice as metastable versus carbide formation.

Three existing potentials for the Fe-C system could be found in the literature. The Johnson potential [49] was composed of pair-potential descriptions for Fe-Fe and Fe-C interactions. However, pair-potentials have well known issues with representing the properties of transition-metals [27]. The Ruda potential [50] has a fatal defect in favoring the tetrahedral over the octahedral configuration for carbon interstitials, contrary to expectations that the solute would prefer the larger interstitial position as confirmed by results from DFT [8, 25]. The most promising potential of the three, according to the comparisons with DFT [8], was the Rosato potential [51], which was created by combining the Johnson Fe-C pair-potential with a superior Finnis-Sinclair (FS) type multibody description of the Fe-Fe interaction [26]. We have however observed that the Rosato potential is unable to duplicate the exact configurations of the 1C-1Va cluster, as detailed in [52]. An energetic description of the C-C interactions is also missing.

3.2.2 Fitting Strategy

Finding a lack of an appropriate potential from the literature, we elect to embark on constructing our own. Realizing the importance of ranking the different minima correctly in comparison to DFT data, we fitted our potential to the energies generated by DFT for specific configurations rather than fitting strictly to energetic data (and ignoring the atomic configuration) as is generally done. To maximize the fitting database and achieve a greater degree of qualitative energy landscape feature correspondence between DFT and the potential, the geometries and respective energies of the relaxed defect clusters, unrelaxed defect clusters and select defect cluster configurations along the CG ionic minimization route were used. We then used the GULP code [1] to fit the potential with the BFGS algorithm to minimize the weighted sum of squares of deviations in calculated

and targeted energies over the parameter space. We elect to employ the relatively simple FS format, where the energy contribution of each atom to the system is

$$E_{\alpha,i} = -A_\alpha \sqrt{\sum_{j \neq i} \rho_{\beta\alpha}\left(r_{ij}\right)} + \frac{1}{2}\sum_{j \neq i} \phi_{\beta\alpha}\left(r_{ij}\right)$$

(For the meaning of the different variables in the equation, refer to Section 2.2.) For the density function and pair-potential parameters of the Fe-Fe term, we adopt the values developed by Finnis and Sinclair, having noticed their ability to match the pure BCC Fe characteristics [53]. For the Fe-C and C-C interactions we use the same form

$$\rho_{\beta\alpha}\left(r_{ij}\right) = t_1\left(r - r_{c,\rho}\right)^2 + t_2\left(r - r_{c,\rho}\right)^3, r \leq r_{c,\rho}$$

$$\phi_{\beta\alpha}\left(r_{ij}\right) = \left(r - r_{c,\phi}\right)^2\left(k_1 + k_2 r + k_3 r^2\right), r \leq r_{c,\phi}$$

where these functions are zero for $r \geq r_c$. The parameters are provided in Table 3.1.

α	β	$r_{c,\rho}$	t_1	t_2	$r_{c,\phi}$	k_1	k_2	k_3
Fe	Fe	3.569745	1	0.504238	3.4	1.237115	-0.359218	-0.038560
Fe	C	2.545937	10.024001	1.638980	2.468801	8.972488	-4.086410	1.483233
C	Fe	2.545937	10.482408	3.782595				
C	C	2.892070	0	-7.329211	22.061824	-17.468518	4.812639	2.875598

Table 3.1: Fitted parameters of the Fe-C potential, assuming units of length in Å and units of energy in eV, where $A_{Fe} = 1.828905$ eV and $A_C = 2.958787$ eV.

3.2.3 Results

Details about the work and the results have been published [52]; we will provide here only a summary of some of the formation energies in Table 3.2 and a commentary on the results.

In general, we find good agreement with DFT for configurations of the highly energetically favorable 1Va-1C and 1Va-2C that were explicitly fitted and reasonable agreement for other defect clusters. The potential also accurately gives the energies of the

Fe$_3$C cementite phase. The potential is however unable to duplicate well the energies of clusters with more than 2 atoms in close proximity to one another, in that the potential assigns far higher energies to these configurations compared to the DFT landscape. Nonetheless, this is to be expected as our representation of the C-C interaction lacks an angular term to describe the highly covalent nature of the C-C bonding. As these defect configurations are generally of higher energy even in the DFT landscape, the misrepresentation of their energies is not particularly serious. And although DFT is biased to the formation of 2Va-4C $\langle 111 \rangle$ clusters unlike the potential, which is biased towards formation of 1Va-2C clusters instead, the stoichiometry of the favored defect species is preserved in the fitting.

| | Formation Energies [eV] | |
Defect Specie	Empirical Potential	DFT
C$_{tet}$	0.78	0.86
1Va+1C	-0.76	-0.53
1Va+2C	-1.73	-1.46
2Va$_{[100]}$	-0.21	-0.18
2Va+1C$_{[100]}$	-1.05	-1.05
2Va+2C$_{[100]}$	-1.65	-1.84
2Va+3C$_{[100]}$	-2.25	-2.31
2Va+4C$_{[100]}$	-3.13	-3.20
2Va$_{[111]}$	-0.14	-0.15
2Va+1C$_{[111]}$	-0.93	-0.80
2Va+2C$_{[111]}$	-1.61	-1.93
2Va+3C$_{[111]}$	-2.39	-2.57
2Va+4C$_{[111]}$	-3.09	-3.62
2Va$_{[4nn]}$	-0.05	0.01

Table 3.2: Formation energies corresponding to the deepest energy minima of different C-Va defect clusters calculated from DFT as described in [25] and obtained from the potential, relative to free vacancies and octahedral C interstitials. A negative energy reported indicates binding. Subscripts on point defect cluster types indicate the sublattice on which the defect species is located. To our knowledge, the only experimental measurements available for comparison are for C$_{tet}$ (0.81 eV [54]) and for 1Va-1C (0.44 eV [55] or 0.85 eV [56]).

Some additional comments concerning our potential could be found in a recent publication [57] describing a newer Fe-C empirical potential constructed using our own fitting strategy.

3.3   Defect Population Spectrum

The diffusivity in a material can be expressed as a function of the properties associated with each relevant discrete diffusive jump mechanism i [6]

$$D^* = \sum_i a_i^2 [i] v_i \exp\left(-\frac{E_{m,i}}{k_B T}\right) f_i$$

where a is the jump distance, $[i]$ is the concentration, v is the jump frequency, E_m is the migration activation energy, and f is the correlation factor. Using this approach, it is necessary to begin by calculating the concentration of the different defect species. Given the variety of defect cluster sublattices that exists in the matrix (e.g. the octahedral sublattice of carbon interstitials), we begin by defining the concentration of point defect clusters (PDC) in relation to the Fe BCC lattice

$$\left[PDC_{PDC-sublattice}\right] = \frac{N_{PDC}}{N_{BCC-lattice}}$$

where N_{PDC} and $N_{BCC-lattice}$ are the number of point defect clusters of species i, PDC$_i$, and of the α-Fe BCC lattice sites, respectively. With the assumption that these PDCs are in local equilibrium with each other and sufficiently dilute to behave ideally, the concentrations of each PDC species can then be expressed as

$$\frac{\left[(xVa - yC)_i\right]}{[Va]^x [C_{oct}]^y} = K \approx \exp\left(-\frac{E_f}{k_B T}\right)$$

where K is the equilibrium reaction constant in the NVT ensemble and E_f is the energy of the formation reaction

$$\left[\left(xVa - yC\right)_i\right] = x\left[Va\right] + y\left[C_{oct}\right]$$

Finally, we constrained the total carbon $\left[C_{tot}\right]$ and vacancy concentration $\left[Va_{tot}\right]$ to be equal to the sum over all PDC species

$$\left[C_{tot}\right] = \sum_i y\left[\left(xVa - yC\right)_i\right]$$
$$\left[Va_{tot}\right] = \sum_i x\left[\left(xVa - yC\right)_i\right]$$

to enable calculation of PDC concentrations for any arbitrary, total concentration of carbon and vacancies[*]. Here, we neglect the vibrational entropic contribution to the equilibrium reaction constant[†].

A few important features can be found from the results of such calculations (the general trends are captured in Figure 3-2). First, the most statistically abundant defect clusters are the monovacancies, divacancies, and 1Va-2C clusters, and as such, are the most important defects to be considered for diffusion in the alloy. In addition, when the total carbon concentration $\left[C_{tot}\right]$ exceeds twice the vacancy concentration $\left[Va_{tot}\right]$, all free vacancies are effectively sequestered with carbon. This is a direct consequence of the strong driving force for formation of 1Va-2C clusters. At a fixed vacancy content, the number of free vacancies and divacancies declines with increasing total carbon content as they serve as reactants to form defect clusters. The concentration of these defect clusters continues to increase with increasing carbon content and saturates when the free

---

[*] It is important that arbitrary vacancy concentrations are permitted in our framework, since the processing and the industrial applications (e.g. fatigue in the 10^9 regime) of these materials mean that the vacancy concentration in the BCC Fe matrix is often unknown (albeit it is certainly higher than is expected from the formation energy and the configurational entropy).
[†] This is to permit the simultaneous idealization of kinetic attempt frequencies of transformations between different PDC species as equal for forward and backward transitions and the maintenance of detailed balance of the defect species concentration.

vacancies are totally exhausted. (The carbon content at which this occurs is when the $[C_{tot}]$ exceeds twice the $[Va_{tot}]$, which is a reflection of the stoichiometry of the favored 1Va-2C cluster.) Further increase in total carbon content serves only to increase the number of carbon interstitials in the material. When the local concentration of carbon $[C_{tot}]$ is less than twice the local vacancy concentration $[Va_{tot}]$, the quantity of free vacancies and divacancies become significant.
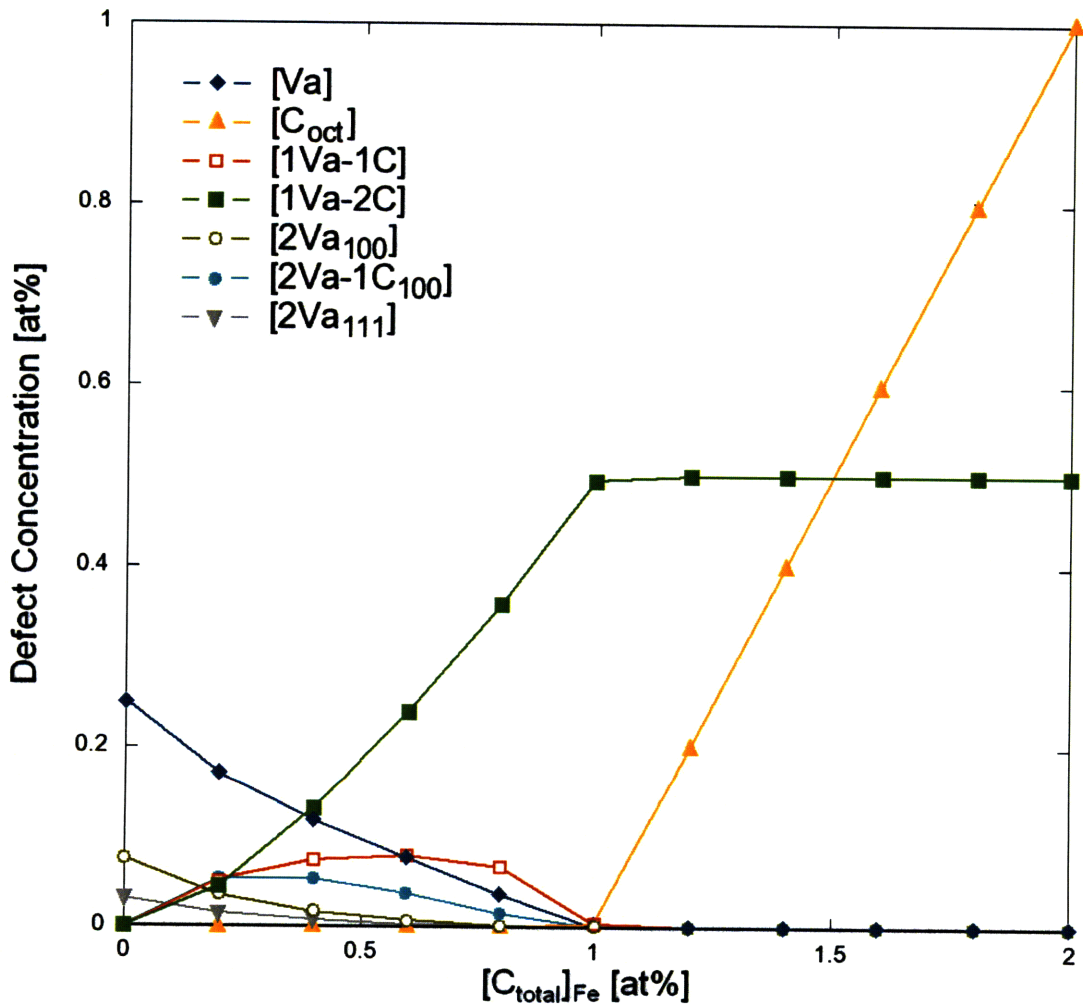
Figure 3-2: Concentrations of various defect species. Calculations were performed at fixed $[Va_{tot}]$ of 0.005 (an arbitrary value) at varying $[C_{tot}]$ for 450 K, as discussed in Section 3.3. Only the most numerically prevalent defect clusters are shown on the plot. The trends, general across any temperature and at any other total vacancy content, are a consequence of the large driving force for defect clusters formation.

3.4   Defect Migration Energetics

Using NEB, we calculated the minimum energy paths and migration barriers for these statistically abundant defects identified in Section 3.3, summarized in Figure 3-3. Migration activation energies E_m were calculated as the difference between maxima and minima of these favored energy paths. The calculated migration barrier of 0.84 eV for a single Fe vacancy agrees reasonably well with that of 0.92 eV obtained from DFT[*]. The calculated migration barrier of 0.81 eV for the divacancy complex 2Va is found to be comparable to that of the monovacancy. The minimum energy path of divacancy migration (see Figure 3-3(b)) includes successive, nearest neighbor jumps of each vacancy, with an intermediate state where vacancies are located at four nearest neighbors positions away. In contrast, the migration of the most statistically abundant PDC, the 1Va-2C cluster, was more complex and of a considerably higher barrier at 2.22 eV. We found the minimum energy path to be a dissociative migration mechanism, whereby the 1Va-2C cluster dissociated into a 1Va-1C cluster and 1C; migration of the intact 1Va-2C cluster was disfavored, with a barrier of 3.21 eV. Due to the considerable mismatch in migration energies between the free mono/divacancies and the 1Va-2C cluster, these carbon-containing PDCs are not expected to migrate or contribute significantly to self-diffusivity at relatively low temperatures ($T < 600$ K), or $T/T_m \leq 0.3$.

---

[*] The experimentalists have been divided into 2 opinions with regards to the vacancy migration enthalpy, with one supporting a value of about 0.55 eV [56] and another supporting a value of about 1.28 eV [58]. Due to this controversy, the values are not included within the main text. A "colorful" discussion that characterizes the opposing camp's data analysis as "kangaroo-court procedure" could be found in [59]; a comparatively dispassionate discussion about the values could be found in [60].
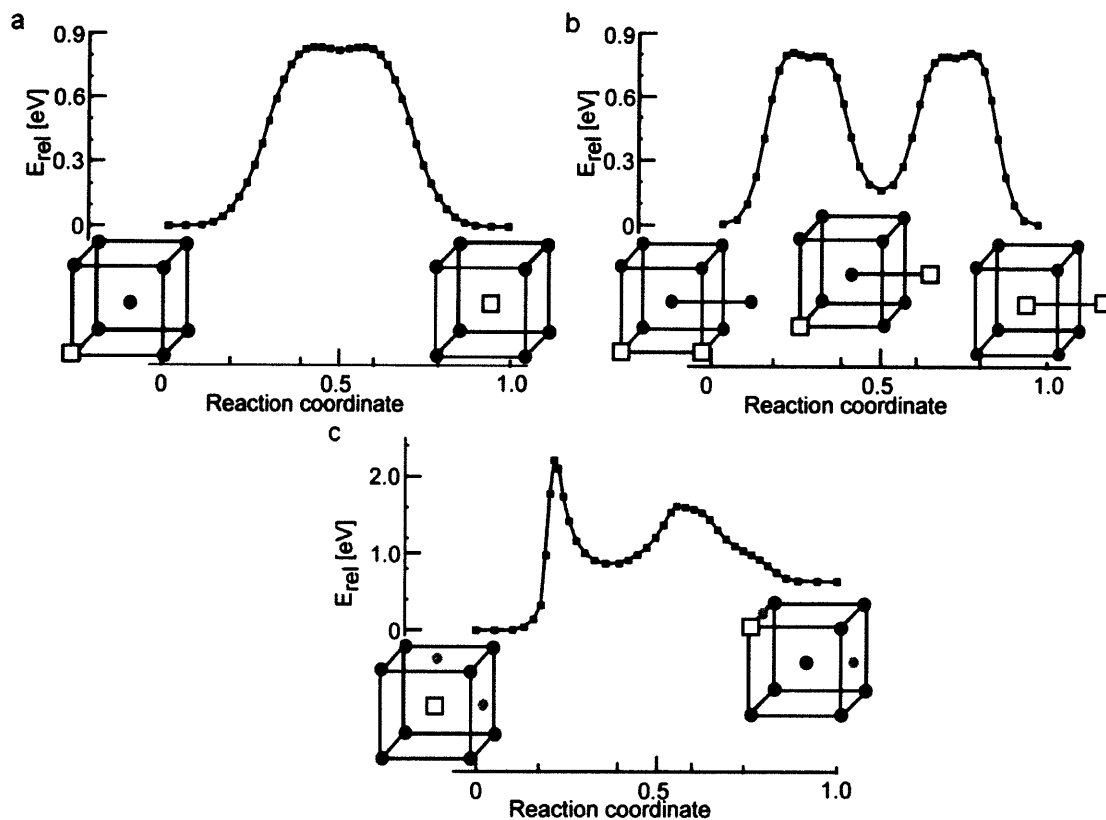
Figure 3-3: Migration energy barriers of the most statistically abundant point defect clusters in BCC Fe-C. (a) Monovacancy; (b) divacancy; and (c) carbon-vacancy cluster in BCC iron-carbon alloy. Relative energy-reaction coordinate pathways are obtained using NEB sampling of minimum energy pathways. Fe atoms are denoted by black circles, Fe vacancies by squares, and C solute by gray circles.

We also computed the full dissociation pathway and migration barriers of 1Va-1C to compare with recently reported calculations [61] although this defect cluster is a less abundant PDC in α-Fe-C alloys by several orders of magnitude (see Figure 3-2 and [25]). The results are given in Table 3.3. That our values are systematically larger by 0.15 eV can be attributed chiefly to different techniques in obtaining the barriers as well as to the use of different empirical potentials to represent the Fe-C interaction. The potential used in this study was specifically developed to accurately predict both the energy and configuration of carbon-rich clusters [52]. Via NEB, we found the migration barrier of this 1Va-1C PDC to be 1.84 eV.

45
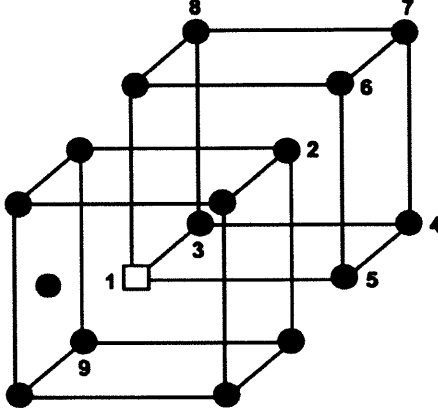
Va Migration	Forward Barrier [eV]		Backward Barrier [eV]	
	This Work	Literature	This Work	Literature
1 → 2	0.60	0.49	0.18	0.28
1 → 9	1.84	1.60	0.87	0.64
2 → 3	0.98	0.79	0.83	0.61
2 → 4	0.81	0.63	0.60	0.47
2 → 5	1.31	0.95	0.96	0.73
2 → 6	0.81	0.63	0.60	0.47
2 → 7	0.86	0.63	0.67	0.50

Table 3.3: Comparison of calculated energetic barriers for stepwise migration of 1Va-1C point defect cluster. Literature results are found in [61]. See text for discussion. Fe atoms are denoted by black circles, Fe vacancies by squares, and C solute by gray circles. The 1 → 4 jump with a maximum barrier height of 1.23 eV in comparison to the deepest energy minimum can be used as an underestimate of the dissociation energy of the cluster, which is experimentally estimated as 1.6-1.7 eV [54].

3.5 Diffusion Rate and Comparison with Experimental Creep Rate

Having identified that the diffusivity is controlled by vacancies and divacancies as the numerically dominant 1Va-2C clusters are essentially immobile while the rate-enhancing 1Va-1C clusters are numerically suppressed, we calculate the Fe self-diffusion coefficient D^*_{Fe} as the sum of the monovacancy (1Va) and divacancy (2Va) migration mechanism [62, 6]

$$D^*_{Fe} = a^2_{Va}[Va]v_{Va} \exp\left(\frac{-E_{m,Va}}{k_B T}\right) f_{Va} + 2a^2_{2Va}[2Va_{<100>}]\left(v_1 \exp\left(\frac{-E_{m,1}}{k_B T}\right) + v_2 \exp\left(\frac{-E_{m,2}}{k_B T}\right)\right) f_{2Va}$$

where a is the jump distance calculated directly from the atomic configurations [6], ν is the jump frequency of the indicated point defect cluster type, f is the jump correlation factor, and subscripts 1 and 2 denote the conversion of the $\langle 100 \rangle$ divacancy to the $\langle 111 \rangle$ configuration and to the intermediate dissociated state at four nearest neighbors distances (see Figure 3-3(b)), respectively. The diffusion parameters, as tabulated according to the methods outlined previously, are summarized in Table 3.4. Divacancy correlation factors were calculated using a functional form given in [63], a fit to Monte Carlo calculations reflecting the dependence on both jump frequency and temperature.

	1Va	2Va$_1$	2Va$_2$
a [Angstroms]	2.482	2.867	
ν_o [THz]	36.73	27.55	9.13
E$_m$ [eV]	0.84	0.98	0.81
f [unitless]	0.72	See Text	

Table 3.4. Diffusion parameters utilized in calculation of D_{Fe}^*. The subscripts referring to the 2 different divacancy moves are described in the text.

Figure 3-4 summarizes the predicted self-diffusivity of BCC Fe comprising 0.5 at. % Va, as a function of total carbon concentration, for three different temperatures. Clearly, Fe self-diffusion depends strongly on the total concentration of Va and C, and on the relative concentration of these two point defect types. When the total carbon concentration $[C_{tot}]$ exceeds twice the vacancy concentration $[Va_{tot}]$, diffusivity is reduced to very low levels ($< 10^{-20}$ cm^2/s). This reduction is a combined effect of the defect mobility and population statistics. As we found from the analysis of barriers (Section 3.4), the vacancies and divacancies are mobile while the 1Va-2C clusters are virtually immobile. Due to the strong driving force for formation of 1Va-2C clusters (as discussed in Section 3.3), in this high carbon regime the mobile vacancies and divacancies are consumed as reactants to form the immobile 1Va-2C clusters, causing an overall reduction in the diffusivity.

This trend, shown in Figure 3-4, for the low-temperature BCC α-Fe phase – decreased self-diffusivity with increased carbon content – is in direct contrast to the experimentally observed effects of carbon on the high-temperature FCC phase, wherein carbon enhances D^*_{Fe} by nearly one order of magnitude upon addition of 1 wt. % C [44]. For the latter alloy, it has been shown that carbon changes the energetics of defect cluster formation and migration in the FCC phase in a complex and fundamental manner: incorporation of carbon also serves to decrease the melting temperature of the FCC alloy, likely due to the magnetic interactions in this FCC phase which is stable above the Curie temperature [46, 64, 44]. Thus it should not be expected that diffusivity in the ferromagnetic BCC ferrite should also increase with an increase in the carbon concentration, particularly as the 1Va-1C mechanisms that enhances self-diffusion in the FCC phase [46] are not dominant in the BCC phase, due to the tendency of carbon and vacancies to form larger, more complex point defect clusters in BCC α-Fe [25]. Moreover, our computational modeling and simulation predictions for the BCC α-Fe phase are consistent with the experimental observations of macroscopic creep strain rates increasing with increasing carbon content as seen in Figure 3-1(b), which operates by the dislocation climb mechanism (in accordance with its power-law stress dependence) and as a result is related to the vacancy diffusion in the lattice [9].
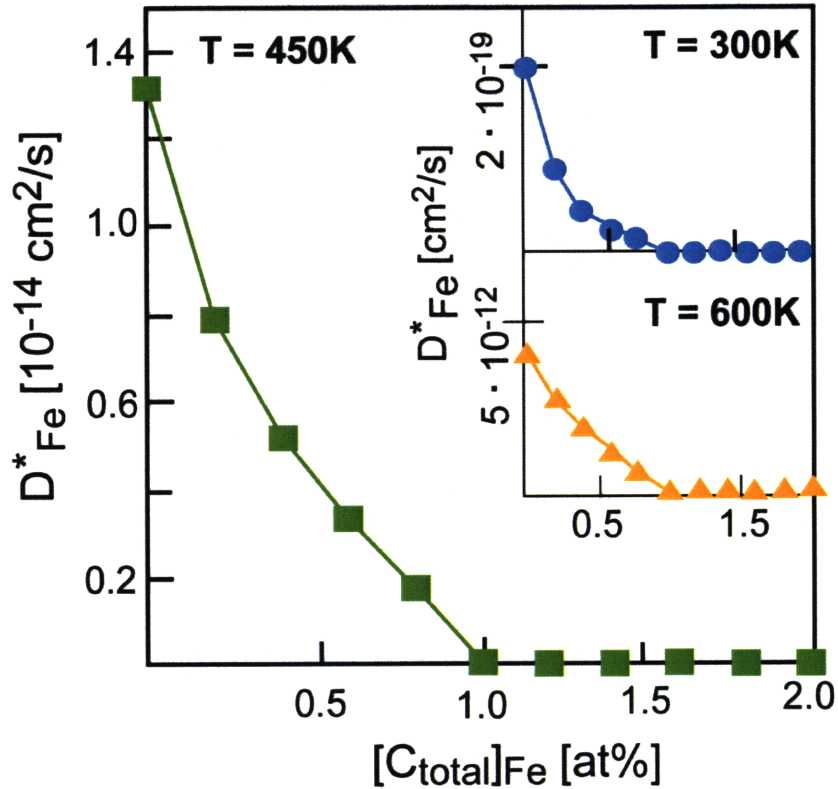
Figure 3-4: Fe self-diffusion coefficient D^*_{Fe} as a function of carbon concentration. For 0.5 at. % vacancies at three operating temperatures (T = 300, 450 and 600 K), diffusivity decreases with increasing carbon content and becomes negligible when carbon concentration exceeds twice the assumed local vacancy concentration.

We thus suggest that the experimental trend in such defected alloys, decreasing creep rate with increasing carbon concentration, can be attributed in part to the reduced number of free-vacancies in α-Fe of increasing carbon content, although a significant fraction of the total carbon content in the alloy is taken up in the Fe_3C carbide particles or sequestered at ferritic dislocation cores [65, 66], and that the local concentration of carbon within the ferritic bulk could differ from the globally measured concentration. More generally though, this modeling and simulation approach, based on analytical predictions from atomistic migration mechanisms and barriers, demonstrates the potential to rapidly survey complex structural alloys for plausible, kinetically controlled deformation mechanisms.

3.6   Extension to Hydrogen-Containing Iron Alloys

Hydrogen is known to have a hardening effect in Fe, which in turn has an impact on the creep behavior. The trapping of H in vacancies is suggested as a possible mechanism for such hardening [67]. We have thus initiated a DFT study on the effect of H in a carbon containing Fe alloy in order to understand the defect interactions and the resultant changes in the defect populations as a starting point.

From our calculations, we found that in an iron alloy with only H solute, there is a strong driving force to forming 2Va-1H clusters (i.e. the reverse of the stoichiometry as the favored defect cluster in iron supersaturated with C), and so when the total hydrogen concentration exceeds half the vacancy concentration, all free vacancies are effectively sequestered with hydrogen. At lower H to vacancy ratios, the numerically prevalent defect cluster transitions from tetrahedral H interstitials (at very low vacancy concentrations) to 1Va-2H to 1Va-1H to 2Va-1H (at high vacancy concentrations). We also find that H atoms are unable to displace C atoms in vacancy-defect clusters, but rather have a tendency to bind to those clusters to form even more complex Va-C-H clusters. The full details of this work as well as the conclusions such defect interactions have on materials properties (e.g. bubble formation) will be included in a forthcoming publication.

4 Vacancy-Dislocation Interaction in BCC Fe

4.1 Past Work

The importance of dislocation climb, the nonconservative motion of line defects out of slip planes via vacancy diffusion to the dislocation core, in the study of creep has long been recognized [11]. As the dislocation climb velocity can be readily related to the material deformation rate, many attempts have been attempted in the past to analytically derive the dislocation climb velocity [11, 68, 12]. However, these modeling attempts face two main challenges. The first is that the equations are very difficult to solve, and as such many factors have to be simplified or ignored. From conventional elasticity theory, it is known that dislocations do have an attractive-repulsive interaction with vacancies [18] due to their stress fields. Due to the difficulty in formulating the equations, for instance, the treatment by Nix *et al.* [12] ignores the angular dependence of the dislocation stress field and the treatment by Weertman [11] ignores the stress field altogether. Moreover, since vacancies have different energies at different lattice sites, it is necessary for the migration barriers to vary for the forward and backward jumps. None of the treatments even attempt to include the effect of a varying migration barrier. So while these treatments all begin with trying to solve a rate problem of a dislocation as a vacancy sink in equilibrium with the bulk vacancy concentration, none of the solutions can claim to satisfy the basic requirement of detailed balance. The second difficulty in these analytic solutions is that many of the quantities that should be included in the treatment simply are not known. For example, it is well-known that elasticity theory cannot treat the core of the dislocation very well [18]. As the dislocation climb problem essentially is one of vacancy binding to the core, the binding energetics of the vacancies to the dislocation

core itself should play a significant role. However, these values cannot be included in the analytic treatments simply because these energies are not known.

With the development of numerical techniques such as kinetic Monte Carlo [69] or continuum transport equation-solving methods such as the finite-element method, the details that understandably were ignored or simplified in the analytic treatments could be included. Atomistic calculations, with the ability to replicate the dislocation down to the individual atoms, are ideal for providing these unknown quantities. Clouet has recently computed the single vacancy energetics as a function of distance from the dislocation core with empirical potentials for a variety of FCC metals [70] and compared the results with elasticity theory. We build upon that perspective to obtain the effect of multiple vacancies in the core and the variation of the vacancy migration barrier as a function of distance from the core in a BCC metal. We also examine the vacancy binding to the dislocation core in order to understand the vacancy interactions within the core region. With these thermodynamic and kinetic parameters of the vacancy migration processes, we illustrate how deviations from mobility within the undefected bulk crystal can be tractably incorporated into numerical simulations of climb.

4.2   Model System

For these simulations, we employed our Finnis-Sinclair type empirical potential for BCC Fe discussed in Chapter 3. We implemented the $\langle 111 \rangle$ (110) 71° mixed dislocation[*] (M111 in the standard notation of Vitek [71]) to facilitate atomistic simulations of an edge-type dislocation with periodic boundary conditions for a reasonable system size and

---

[*] It is well known from conventional elasticity theory that vacancies would be attracted to edge dislocations and not screw dislocations. The choice of the mixed dislocation is made out of a principle of choosing a dislocation line direction that is a nearest neighbor direction (i.e. $\langle 111 \rangle$) and which maximizes the edge character. The pure edge dislocation (EDGE in the standard notation of Vitek [71]) has a line direction of $\langle 121 \rangle$.

associated computational expense. A monoclinic periodic supercell was constructed with boundaries in the directions of $[111]$, $[\bar{1}1\bar{1}]$, and $[\bar{1}01]$, extending over 40, 10, and 40 lattice layers, respectively. Dislocations were generated by removing planes of atoms along the line direction of $[\bar{1}1\bar{1}]$ (similar to the dislocation generation method employed in [72]). To simulate the dislocation quadrupolar array[*], the 40 × 10 × 40 supercell was mapped to a new supercell that contained only half as many atoms [74]. Two different dislocation core configurations are necessarily present in our constructed quadrupolar array described above, as illustrated in Figure 4-1. We refer to the atom-centered dislocation as AD (the M111 structure as identified by Yamaguchi et al. [75]) and the bond-centered dislocation as BD. In a separate dipole calculation (which permits isolation of each dislocation type) we have confirmed that both structures are stable and found that the AD is slightly more energetically favorable than the BD by 44.1 μeV/Å[†]. In this work we chose to focus on the AD core explicitly.

All structural and supercell relaxations were performed by using the CG as implemented in the GULP code [1]. The minimum energy paths between these energetically minimized structures were computed with the NEB method implemented in GULP. Throughout this work the interaction energy between the Nth vacancy and a dislocation with N-1 vacancies is defined as

$$E_{V-D}^{inter} = \left(E + E_{V-D} \right) - \left(E_D + E_V \right)$$

---

[*] Periodic dipolar systems are generally more convenient for simulations involving edge dislocations, since dislocations of the opposing polarity would in this case not be placed on the exact same glide plane and the risk of dislocation annihilation during the simulations can be avoided. However, due to the long range of the dislocation stress fields, which decays to $1/R$ according to distance R [18], the sum of the stress fields of dislocations in a periodic dipolar system is only conditionally convergent. While there are techniques using elasticity theory as a basis to allow for calculations of local stresses and dislocation core energies, how, or whether at all, the same could be done for energy barriers, the subject of this study, is not clear. The issue is entirely side-stepped by the use of a periodic quadrupolar system, in which the sum of the stress fields of dislocations is absolutely convergent. A discussion of the issue can be found in [73].
[†] The BD could be thought of as the midpoint configuration during glide, and the small difference is consistent with the low Peierls stresses associated with BCC edge-type dislocations [76, 77].

where E, E_V, E_D, and E_{V-D} refer to the energies of the pure bulk, of the bulk with one vacancy, of the dislocation simulation cell with N-1 vacancies, and of the dislocation simulation cell with N vacancies [70]. A negative value of E_{V-D}^{inter} thus indicates vacancy attraction to the dislocation core.
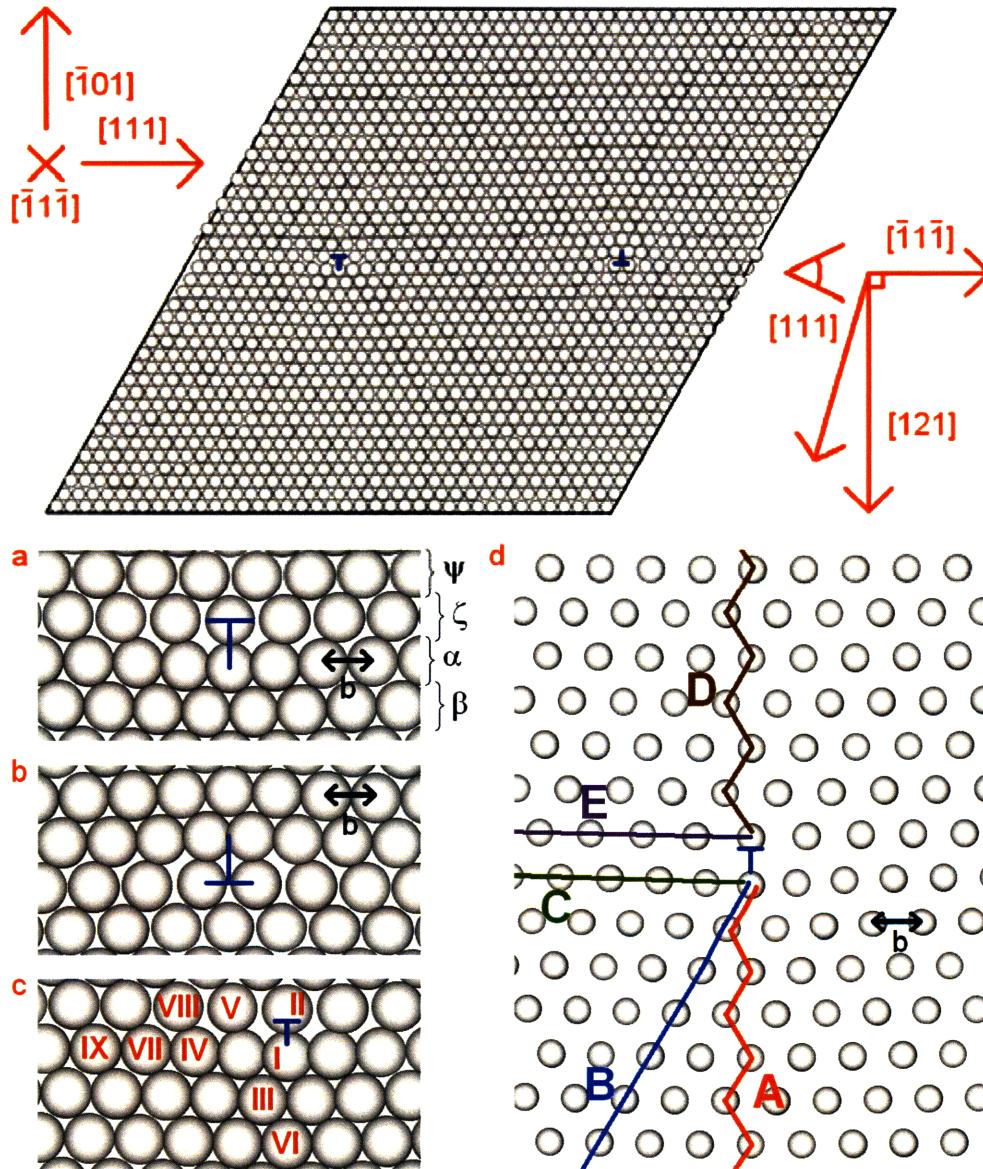
Figure 4-1: Quadrupolar system containing two different dislocation core configurations. (a) An atom-centered core. (The Greek letters define planes referred to in subsequent discussions.) (b) A bond-centered core. (c) Various positions around the core as referred to in Table 4.2. (d) Five (A, B, C, D, and E) possible pathways of vacancy movement towards the core referred to in the text. Figure generated with Atomeye [78].

4.3 Unit Processes of Dislocation Climb

The unit mechanisms of climb can be roughly divided into two types, that of the vacancy binding to the core itself and that of the vacancy movement from distance towards the core. We will discuss these two in turn.

4.3.1 Vacancy-Core Binding and Evolution of Dislocation Structure

At the atomistic level, the unit process of climb is initiated by the binding of a vacancy to the core, and climb of a given segment is complete when enough vacancies bind to the core to move the entire dislocation line one step normal to the glide plane. We find that significant variation exists among the incremental binding energies of the vacancies to the dislocation core that initiate, continue, and complete the climb event. The results are summarized in Table 4.1, which indicates that the interaction energies range from -1.13 eV to -2.19 eV with a mode of -1.8 eV. (The -1.13 eV required for the initial binding can be compared with -0.92 eV [79] obtained for the EDGE dislocation.) This provides a simplification in dislocation climb simulations; namely, the binding of vacancies to the core during climb may be modeled by three separate events: the creation of a jog by the binding of a vacancy to the dislocation core (Figure 4-2(a)), the increase in jog length by an additional vacancy bonding to the line of vacancies in the core (Figure 4-2(b)), and the coalescence of two different jogs (Figure 4-2(c)).
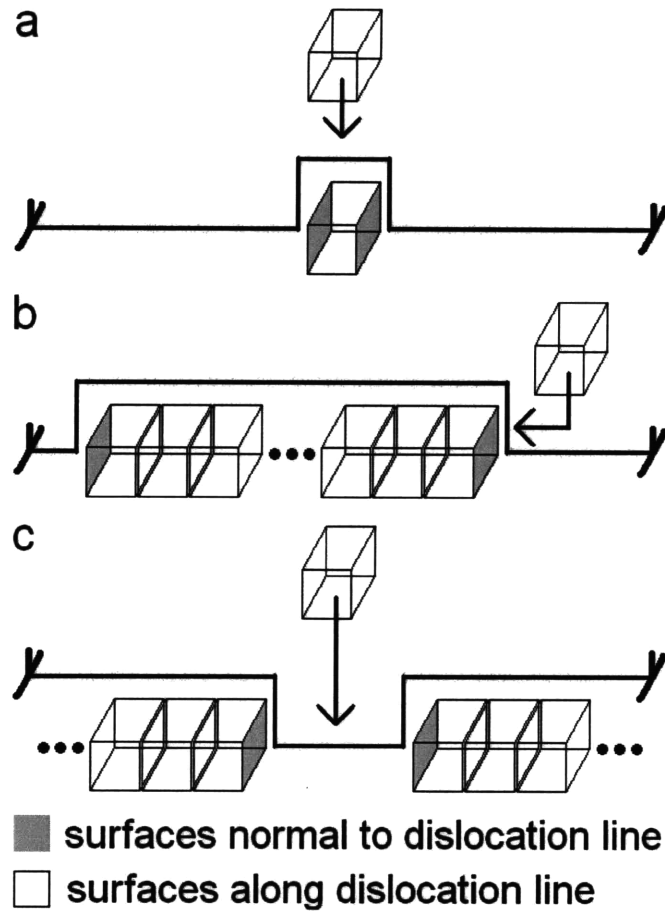
Figure 4-2: Atomistic schematic of climb. (a) The initiation of a jog by the binding of a vacancy to the dislocation line. (b) The expansion of the jog by binding of a vacancy to the end of a line of vacancies in the core. (c) The coalescence of two discrete jogs. The line direction of the dislocation system in this work is $[\bar{1}1\bar{1}]$.

These trends illustrate the particle adsorption nature of vacancy binding to the dislocation core and could be rationalized as a surface change within the dislocation core. The first vacancy that joins the dislocation core and forms the jog introduces extra line length or "surfaces" (with the length scale of a nearest neighbor distance) along the line direction and also creates 2 terminal jog surfaces normal to the dislocation line direction. Subsequent vacancies joining the core continue to expand the jog, adding surfaces along the dislocation line but leaving the number of terminal jog surfaces unchanged. The last vacancy that joins the dislocation core and coalesces two jogs adds surfaces along the

dislocation line but also removes the two terminal jog surfaces at either end of the jogged segment. While this conceptualization grossly simplifies the exact nature of vacancy binding to the dislocation core, it is consistent with our calculations in two ways. First, from the consideration of the surfaces created, the energy required to increase the jog length by the bonding of one vacancy to the line of vacancies in the core should be equal to half of the sum of energy of initiating the jog (here, -1.13 eV) and of the energy of the coalescence of two jogs (here, -2.19 eV), or -1.66 eV. This estimate agrees well with the calculated result of -1.8 eV. Second, this model also predicts that the energy released when a vacancy joins two distinct jogs to form a single, longer jog should exactly match the energy released when a climb event is completed. We obtained the energy of the binding of a vacancy to two adjacent jogs of two vacancies each to form a jog of five vacancies as -2.33 eV. This agrees reasonably well with that calculated for the completion of a climb event (-2.19 eV), confirming the validity of the approximation.

N	E_{V-D} [eV]	N	E_{V-D} [eV]
0	-1.13	5	-1.81
1	-2.01	6	-1.82
2	-1.86	7	-1.80
3	-1.82	8	-1.78
4	-1.81	9	-2.19

Table 4.1: Interaction energy of dislocation core with N vacancies already bound to the core with a single free vacancy in bulk. As there are 10 lattice layers along the dislocation line direction of $[\bar{1}1\bar{1}]$ in our supercell, there are 10 values in the table.

4.3.2 Vacancy Away from the Core

Difficulties in the fundamental understanding of dislocation climb are due to the slow dynamical nature of this collective process; explicit treatment of the nature of dislocation climb ought to address the energetic details (both thermodynamic and kinetic) of vacancies as a function of distance from the core. As shown in Figure 4-3 for a specific vacancy diffusion path (path A in Figure 4-1(d)), we found that the energetic minima of

one single vacancy at different lattice site distances from the dislocation core can be well described by both isotropic [18] and Stroh anisotropic [80] elasticity theories, provided the vacancy and dislocation core are far apart (here, four Burgers vectors). This success of elasticity theory in predicting vacancy energetics away from the core is in qualitative agreement with Clouet's observations for FCC metals [70]. Figure 4-3 also indicates that, in the region where the elasticity theory holds, the magnitude of the interaction energy is typically small (~ 0.05 eV). This trend is consistent with the results of Kamimura et al. [79] for the EDGE dislocation type (in the notation of Vitek [71]) using the same empirical potential. This result shows that vacancies interacting with edge-type dislocation cores can be treated as free vacancies subjected to the elastic field of a dislocation. Explicit atomistic treatment is necessary only when vacancies are a few Burgers vectors away from the core, as well established by the principle of the core cut off radius in elastic treatment of dislocations.

As shown in Figure 4-3, the migration barriers of the single vacancy towards the core converges to the vacancy migration barrier in the perfect lattice at approximately four Burgers vector distances from the dislocation core. Similar trends are found for the other four migration paths specified in Figure 4-1, with relevant variations highlighted in Figure 4-4(a). The vacancy migration barriers for diffusion parallel to the dislocation line length show similar behavior as well (Table 4.2). We note that the significant differences between the paths imply that any attempt to model the near-core vacancy behavior should not ignore the angular dependence of the paths in relation to the core that is neglected for purposes of simplification in analytic studies of climb [11, 12].
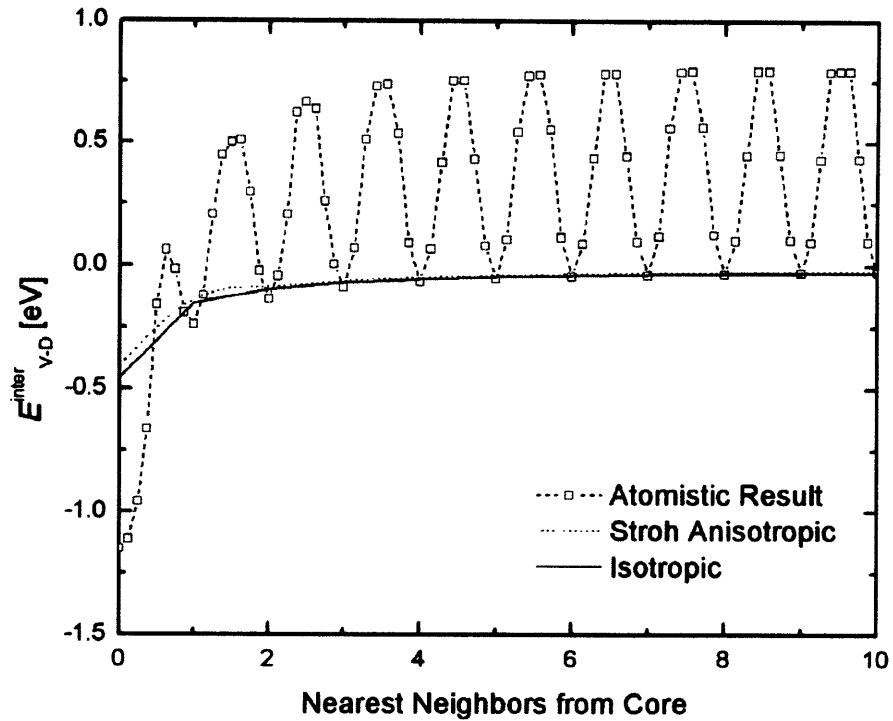
Figure 4-3: Vacancy and dislocation core interaction energy as a function of the number of nearest neighbor jumps of the vacancy away from an otherwise "pure" dislocation core in Path A, relative to a vacancy in a pure bulk. Values at whole numbers of jumps represent the energies of vacancies at an atomic site obtained by conjugate gradients minimization. These are to be compared with the predictions of elasticity theory and with the findings of Clouet [70]. We further include the energy barriers that arise from movement of the vacancy between discrete lattice points, where the points between whole numbers jumps represent the minimum energy path for the jump obtained by the NEB method and the peaks correspond to the migration barriers. For reference, the migration of the vacancy in bulk is 0.84 eV (see Figure 3-3(a)).

Position	$E_{barrier}$ [eV]
I	1.29
II	0.87
III	0.70
IV	0.57
V	0.96
VI	0.84
VII	0.70
VIII	0.89
IX	0.79

Table 4.2: The migration energy of vacancies parallel to the dislocation line direction of $[\bar{1}1\bar{1}]$ at various positions around the core as defined in Figure 4-1(c). These values also show the convergence seen for the migration towards the core towards the bulk migration energy of 0.84 eV (see Figure 3-3(a)) within four Burgers vector distances from the core.
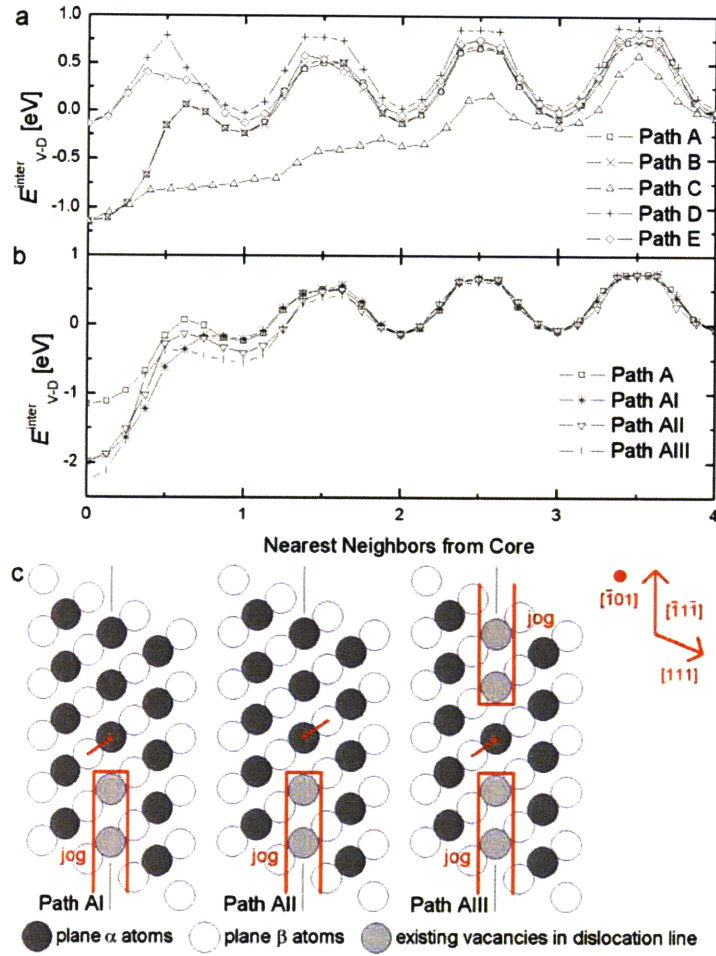
Figure 4-4: (a) Interaction energy of a pure dislocation and a single vacancy as a function of the number of nearest neighbor jumps of the vacancy away from the otherwise unjogged dislocation core for paths specified in Figure 4-1(a), relative to a vacancy in a pure bulk. The points between whole numbers of jumps mark the vacancy migration energies. Note that Paths A, B, and C are on the compressive side of the dislocation core, while Paths D and E are on the tensile side of the dislocation core. The difference between the compressive and tensile nature gives rise to two distinct values for E_{V-D}^{inter} at the 0th nearest neighbor from the core. For reference, the vacancy migration barrier from the core position on the compressive side to the core position on the tensile side (i.e. from position I to II in Figure 4-1) is 1.73 eV. (b) Interaction energy between an unjogged dislocation segment and a single vacancy versus the number of nearest neighbor jumps of the vacancy away from an otherwise unjogged dislocation core in paths specified in (c), relative to a vacancy in the pure bulk. For Paths AI and Paths AII, the vacancy joins another vacancy in the core to form a line of two vacancies at the core. For Path AIII, the vacancy joins two separate lines of 2 vacancies each to form a continuous jog of 5 vacancies in the core. The energetics of the single vacancy traveling on Path A is included as well for comparison. (c) Paths AI, AII, and AIII referred to in (b). Refer to Figure 4-1 for definitions of paths and planes.

It is also of interest to investigate cases of the migration energies of vacancies toward jogged dislocation segments (i.e. vacancies are bound to the core). Taking Path A as an example, we identify three variations that arise from the loss of translational symmetry along the dislocation line as a result of the presence of vacancies within the core (Figure 4-4(c)): two for the extension of the jog by vacancy binding (AI and AII); and one for the coalescence of two jogs (AIII). The results of the vacancy energetics along the paths can be seen in Figure 4-4(b). We observe that the barriers of migration to the core only significantly vary from the monovacancy case within one nearest neighbor distance from the core. This result suggests that perturbations within the core have a very short-range effect, as compared to the dislocation strain field itself, on the energetics of vacancies approaching the core. Such quantitative observations significantly reduce the amount of information needed to be tabulated from atomistics and transferred to kinetic simulations, as the kinetics of the monovacancy case can be used to be representative of the general vacancy interactions with jogged or unjogged dislocation segments, except for interactions in which the vacancy is one nearest neighbor from the dislocation core.

4.4   Modeling Dislocation Climb and Calculating the Climb Rate

From the previous section, we draw three general conclusions about the vacancy interaction with a dislocation core and its migration behavior near this core. First, the vacancy core binding energetics can be approximated as an adparticle modification of the dislocation core. Second, significant differences in the energetics and migration barriers of the vacancies around a dislocation core from the free vacancy behavior occur in a vicinity of a few Burgers vector $|\vec{b}|$ distances from the core ($4|\vec{b}|$ for this dislocation in BCC Fe). Third, the energetics and migration barriers of the monovacancy binding to the core can be taken as representative of vacancy binding to a jogged core containing an

arbitrary number of vacancies, except in the very last unit process of vacancy binding directly to core. These details by themselves however cannot yield the dislocation climb velocity. For that purpose, the use of another numerical method to calculate the rate by integrating over the different diffusion pathways is needed. How to insert these atomistic details into these integrators greatly depends on the algorithm used; in this section, we will describe specifically how to incorporate such details into kinetic Monte Carlo (kMC) simulations of dislocation climb.

The kMC method [81] begins with the formulation of an event list of possible transitions from an initial state. The system is permitted to evolve to one of these transitions with a probability proportional to the rate of the specific transition (which depends on the barrier for the transition). The elapsed time for this occurrence is

$$\Delta t = \sum_{processes} \frac{1}{rate_{process}}$$

With the details of the energy saddle points for our dislocation climb problem, the kMC method is ideally suited for our problem. We replicate the material using a regular BCC lattice system, with all diffusive moves represented with nearest neighbor atom swaps[*]. To duplicate the edge dislocation in this lattice representation, we again utilize the concept of cutting out a plane (as discussed in Section 4.2), which we accomplish by treating atoms on opposites of the cut plane as nearest neighbors. A schematic of this method can be seen in Figure 4-5. The vacancy energetic barriers presented in Section 4.3 are referenced in a table look-up according to the location of the vacancy in relation to the dislocation.

---

[*] kMC simulations involving dislocations are typically conducted using the discrete dislocation dynamics approach where the dislocations are represented by discretized line segments and the atoms are entirely abstracted away. An example of such a simulation where dislocation climb and glide are simultaneously addressed can be found in [82]. Our desire to include the details of the energy saddle points and of discrete atomic jumps in a detailed simulation of climb however means that we cannot coarse-grain the lattice; hence the use of an alternate approach.
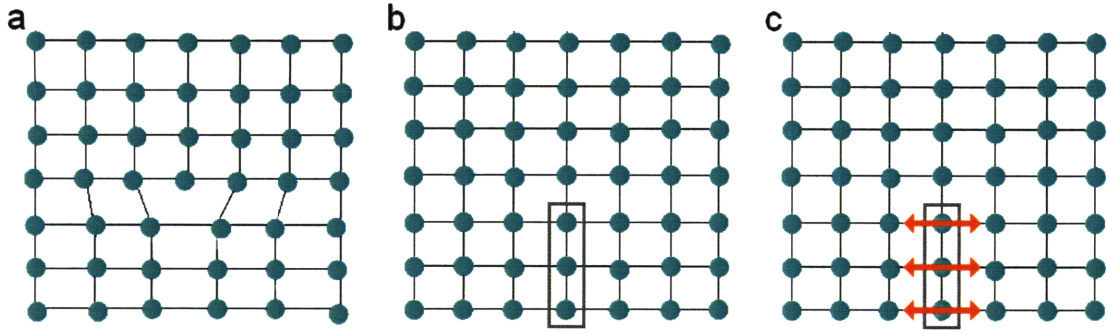
Figure 4-5: The scheme to represent an edge-type dislocation in a regular lattice for kMC simulations. (a) The edge dislocation to be simulated. (b) The regular lattice, with the plane outlined in gray which must be removed to simulate the edge dislocation in (a). (c) The conceptual removal of this additional plane by creating the nearest neighbor relationships signified by the arrows.

Using this approach, we are able to calculate the rate of vacancy binding (to the core) as well as the rate of energy dissipation[*]. By the combination of these rates, we are able to obtain the dislocation climb velocity [12], and by extension, the material creep rate [10]. This approach is also open to future extension to incorporation of dislocation glide as well as of the influence of solutes simply by expansion of the event list. The full details of this work will be included in a forthcoming publication.

---

[*] The chemical potential of the vacancy varies as a position of the vacancy in relation to the dislocation. As a result, every vacancy jump involves either the absorption or dissipation of energy.

5 Cation Diffusion in Nonstoichiometric $Fe_{3-\delta}O_4$ Spinel

5.1 Past Studies

5.1.1 Oxide Layer on Fe Structure and Its Relation to the $Fe_{3-\delta}O_4$ Spinel

Experimental investigations have been conducted into the structure of the thin films of oxide on the surface of iron [13, 83] as well as on the surface chemical reactions [84]. These studies suggest that the oxide has a spinel structure, but the material is neither of the well-known spinel iron (mineral) oxides of magnetite (Fe_3O_4) and maghemite (γFe_2O_3) [13]. However, from the statistics of the occupation of the various cation positions of the spinel structure in the surface oxide [85], it is understood that the film is most closely related to magnetite (Figure 5-1).

As diffusion of metal cations from the metal bulk through the oxide layer to the surface is necessary to sustain the continual oxidation of the metal, knowledge of the nature of transport in the oxide is important to construct a description of the overall kinetics of oxidation. To this end, we will investigate the cation transport, in terms of the atomic pathways and activation energies, in the related material of nonstoichiometric magnetite $Fe_{3-\delta}O_4$ as a starting point for understanding the properties of the oxide layer. This is because magnetite is much better characterized and known[*], and there exists a bulk of experimental studies into the phase stability, deviation from stoichiometry, and diffusivities of magnetite for comparison with our calculations.

---

[*] Only the statistics of the site occupation in the surface oxide structure is determined, the precise atomic configuration, or even the exact stoichiometry, is not known [13].
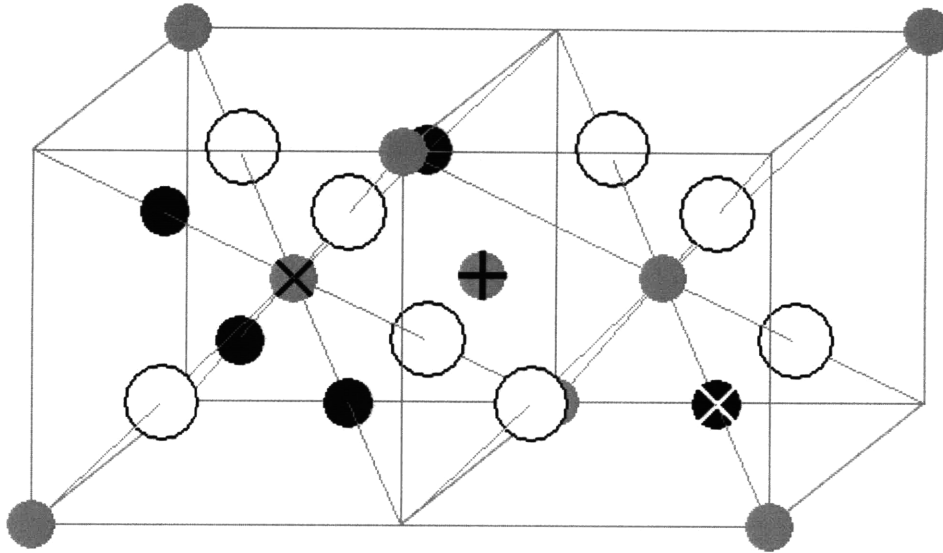
Figure 5-1: The primitive cell for the $Fe_{3-\delta}O_4$ spinel. The black and gray atoms represent Fe atoms in octahedral and tetrahedral positions respectively and the white atoms represent O atoms. Following the standard notation [86], the gray atom with the vertical cross will be referred to as a type B tetrahedral interstitial while the gray atom with the diagonal cross will be referred to as a type C tetrahedral interstitial. The black atom with the cross refers to an octahedral interstitial.

5.1.2 *Previous Experimental Studies of Diffusion in $Fe_{3-\delta}O_4$*

A vast experimental collection of data related to cation transport in magnetite has been assembled. The experimental Gibbs free energy of formation of magnetite has been well determined by a number of different methods [87, 88]. The deviation from stoichiometry δ of $Fe_{3-\delta}O_4$ has also been determined as a function of temperature and of oxygen activity [19], an example could be seen in Figure 5-2. These data yield the defect population, which permits the calculation of the equilibrium constants for the vacancy formation reactions

$$3Fe^{2+} + \frac{2}{3}O_2 \rightleftharpoons 2Fe^{3+} + Va_{Fe} + \frac{1}{3}Fe_3O_4\,(\mathrm{srg})$$
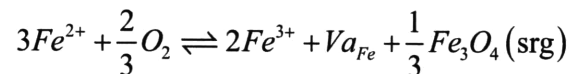
as well as the interstitial formation reaction

$$Fe^{n+} + 2Fe^{3+} + \frac{1}{3}Fe_3O_4\,(\text{srg}) \rightleftharpoons \frac{2}{3}O_2 + Fe_{\text{int}}^{n+} + 3Fe^{2+}$$
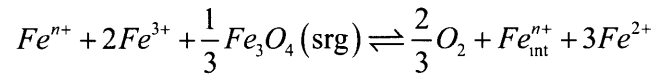
where the units of Fe_3O_4 involved in the reaction are located at sites of repeatable growth (srg, e.g. grain boundary). These equilibrium constants in turn yield the Gibbs free energy of defect formation.
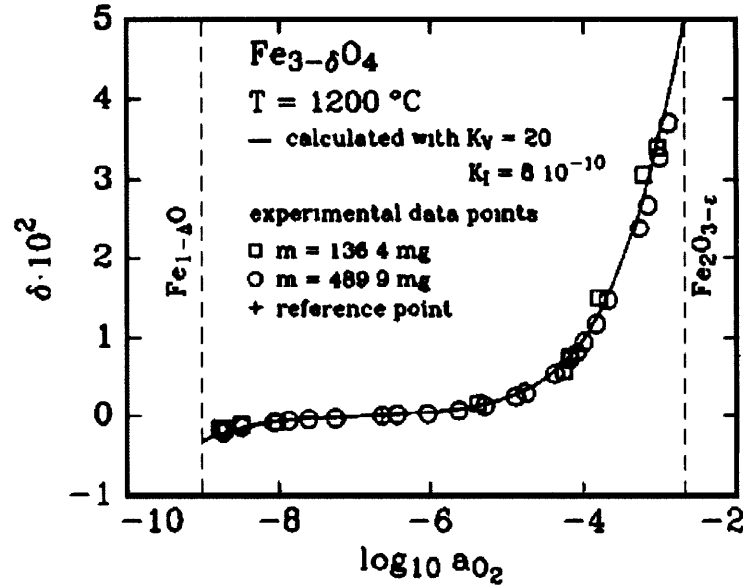
Figure 5-2: Experimentally measured deviation from stoichiometry δ in $Fe_{3-\delta}O_4$ at 1473 K as a function of oxygen activity. The free energy of formation of defects could be inferred from such data. (Figure 10 of [89].)

Measurements of diffusivities in magnetite have also been made as a function of temperature and of oxygen activity [20], as seen in Figure 5-3. Coupled with the information of the defect structure mentioned above, the properties of the defect diffusion could be deduced.

Despite the abundance of data in this area, these experiments cannot alone provide mechanism-specific understanding of the oxide. This is because the techniques can usually only provide an integral measure of aggregate defect properties without the ability to discriminate between the different types of defects or the diffusion mechanism of each defect type [89]. This is particularly problematic in a complicated microstructure

such as magnetite, where the number of defect types is large. For instance, while experimental data can provide some vacancy diffusion activation energy for magnetite, they cannot reveal (without ambiguity) whether that value is a property of the tetrahedral or of the octahedral vacancy type (see Figure 5-1).
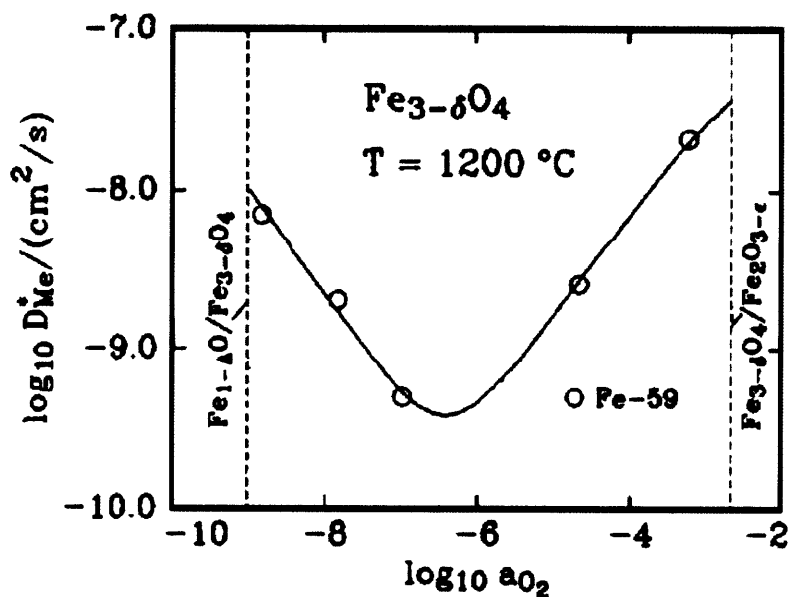
Figure 5-3: Experimentally measured cation diffusivity in $Fe_{3-\delta}O_4$ at 1473 K as a function of oxygen activity. (Figure 10 of [89].)

There is therefore great value in using computer simulations, where each defect type can be isolated for individual study, to help clarify the understanding of the defect migration in magnetite.

5.1.3   Previous Computational Studies of Diffusion in $Fe_{3-\delta}O_4$

As magnetite exhibits complicated electronic properties (e.g. the Verwey charge-ordering first-order transition) that are still poorly understood, there has been intense interest in using computer modeling to calculate the electronic and magnetic properties [90, 91] or oxidation energies [92] of magnetite. While these studies are mostly irrelevant to our study, they do demonstrate the viability of using DFT as an energy landscape to study

magnetite, albeit with the use of a Coulomb interaction correction. (This so-called "+U" correction is devised to help with the treatment of the Coulombic repulsion between d and f electrons localized at ionic cores[*], details of the formulation can be found in [94].) There has been much less interest in the study of cation transport in the structure. The most significant is a catalogue of the different possible diffusive defect pathways and the calculation of their respective correlation factors with Monte Carlo [86]. A DFT study (without the +U correction) has also been used to study vacancy migration in magnetite [95]. However, this study made no effort to benchmark their results against DFT+U calculations, known to be more reliable (if not critical) in modeling the oxide, and has not considered the diffusion of interstitials. An empirical potential based atomistic investigation of the energetic barriers of diffusion in magnetite has also been conducted [96]. While [96] is far more comprehensive in comparison with [95] in terms of exploring the different defect pathways as listed in [86], the results however are found to agree very poorly with experiments [96, 20]. This is not surprising since empirical potentials are hardly expected to be able to capture the energetics resulting from the subtle electronic effects in play within the material. We thus seek to expand on the existing studies by investigating both the vacancy and interstitial diffusion mechanisms in a more complete manner with DFT.

5.2   Calculations of Defect Formation and Migration Energetics

The DFT calculations were performed using the VASP package, as mentioned in Section 2.2. The calculations are performed in essentially the same way as in [25], with the

---

[*] This is the well known Mott insulator problem in solid state physics [93]. Electronic structure methods (which DFT is a member of) do not fully address the details of the electron-electron interactions, but rather do so in an averaged way. They therefore suffer weaknesses where these effects are important, where, for example, in certain transition-metal oxides they predict metals where insulator properties are expected.

parameters for the +U calculations taken from [92]. (In the rest of the text, calculations done without the +U formalism will be referred to as "regular DFT" to avoid ambiguity.) Calculations for $Fe_{3-\delta}O_4$ were performed in 1 unit cell of 56 atoms at fixed volume with the equilibrium lattice constant calculated for each of the energy models (8.4 Å for regular DFT and 8.53 Å for DFT+U respectively). In our calculations, the 3p electrons of Fe are treated as valence states. For transition-state calculations, the climbing image NEB [35], a variant of the basic formulation mentioned in Section 2.3.2 where the image with the highest energy is manipulated to converge onto the saddle point, is used.

To connect our results with experimental values, it is necessary to calculate Gibbs free energies. For the condensed phases, the Gibbs free energy, without the configurational entropy, at some given temperature T, reference pressure, and oxygen activity could be expressed as

$$G\left(T, P^{\circ}, a_{O_2}\right) = E + k_B T \sum_{atoms} \ln\left(1 - \exp\left(-\frac{\hbar\omega_{atoms}}{k_B T}\right)\right) + \sum_{atoms} \frac{\hbar\omega_{atoms}}{2}$$

where E is the energy of the configuration generated from DFT with reference to individual atoms in vacuum. The vibrational contribution has been approximated by treating each atom as a three-dimensional harmonic oscillator with vibrational frequency ω, and the PV term has been neglected. The Gibbs free energy of each O_2 molecule is expressed as

$$G\left(T, P^{\circ}, a_{O_2}\right) = E + \frac{\hbar\omega}{2} + k_B T \left[\begin{array}{c} -\ln\left(\left[\frac{2\pi m k_B T}{h^2}\right]^{\frac{3}{2}} \frac{k_B T}{P^{\circ}}\right) \\ +\ln\left(1 - \exp\left(-\frac{\hbar\omega}{k_B T}\right)\right) - \ln\left(\frac{2I k_B T}{2\hbar^2}\right) + \ln a_{O_2} \end{array} \right]$$

where I refers to the moment of inertia of the molecule. The Gibbs free energy of a reaction can thus be obtained from the DFT results as

$$\Delta G\left(T,P^{\circ},a_{O_2}\right)=\Delta_{O_2}+\sum_{products}G_{products}\left(T,P^{\circ},a_{O_2}\right)-\sum_{reactants}G_{reactants}\left(T,P^{\circ},a_{O_2}\right)$$

Δ_{O_2} refers to the correction of -1.36 eV per O_2 molecule as reactant suggested for DFT+U [92] but which appears to be needed for regular DFT as well.

The Gibbs free energy of the formation reaction of pure magnetite

$$3Fe\left(\text{BCC}\right)+2O_2 \rightleftharpoons Fe_3O_4$$
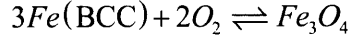
has been calculated with regular DFT. A fit of ΔG of $-11.67eV+0.00325\dfrac{eV}{K}T$ was obtained from calculations with a reference pressure of O_2 at 1 bar, matching closely with the experimental measurement of $-11.50eV+0.00339\dfrac{eV}{K}T$ [87].

We use the DFT Gibbs free energy result of the vacancy formation reaction

$$Fe_3O_4\left(\text{perfect}\right)+\frac{2}{3}O_2 \rightleftharpoons Fe_3O_4\left(\text{with vacancy}\right)+\frac{1}{3}Fe_3O_4\left(\text{perfect}\right)$$

to approximate the Gibbs free energy result of

$$3Fe^{2+}+\frac{2}{3}O_2 \rightleftharpoons 2Fe^{3+}+Va_{Fe}+\frac{1}{3}Fe_3O_4\left(\text{srg}\right)$$
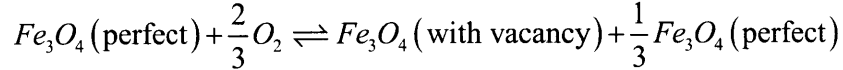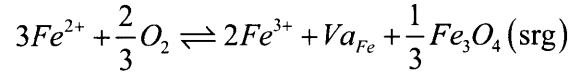
for both the octahedral and tetrahedral vacancies. Likewise, the DFT Gibbs free energy result of the interstitial formation reaction

$$Fe_3O_4\left(\text{perfect}\right)+\frac{1}{3}Fe_3O_4\left(\text{perfect}\right)\rightleftharpoons\frac{2}{3}O_2+Fe_3O_4\left(\text{with interstitial}\right)$$
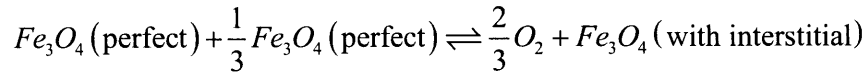
is used to approximate the Gibbs free energy result of

$$Fe^{n+}+2Fe^{3+}+\frac{1}{3}Fe_3O_4\left(\text{srg}\right)\rightleftharpoons\frac{2}{3}O_2+Fe_{\text{int}}^{n+}+3Fe^{2+}$$
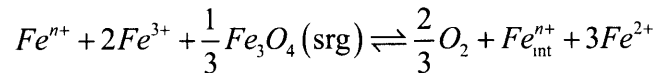
for all interstitial types.

The reason for this simplification is because the charge associated with each ion is not a well defined quantity in quantum mechanical calculations[*]. In our calculations, we permit the electronic degrees of freedom to fully relax, and we do not discriminate between the possible valences the interstitials can adopt. The energies we tabulate for the interstitials are strictly for the case where the interstitials adopt the valence state which minimizes the system energy. This is a serious omission, which we acknowledge but cannot avoid. (How the charge state of an ion affects its diffusivity is at present unknown, see [89] for a discussion on an experimental point of view.)

5.2.1 Defect Formation

The results for the defect formation calculations are summarized in Table 5.1.

Defect Specie		Regular DFT		DFT+U	
		A [eV]	B [eV/K]	A [eV]	B [eV/K]
Fe Vacancy	Octahedral	-2.94	0.00107	-2.95	0.00115
Fe Vacancy	Tetrahedal	-1.05	0.00109	-1.84	0.00117
Fe Interstitial	Octahedral	7.12	-0.00138	6.72	-0.00122
Fe Interstitial	Oct. Dumbbell	6.6	-0.00091	N/A	N/A
Fe Interstitial	Tetrahedral, Type B	6.78	-0.00107	6.87	-0.00108
Fe Interstitial	Tetrahedral, Type C	9.39	-0.00101	10.9	-0.00132
Fe Interstitial	OOTV	N/A	N/A	5.87	-0.00112

Table 5.1: Gibbs free energy of defect formation reactions at the reference pressure of O_2 at 1 bar calculated with and without the +U formalism. A is the 0 K formation energy and B is the formation entropy obtained by fitting the calculated Gibbs free energy to the form $\Delta G = A + BT$. Formation energies calculated with +U for the octahedral dumbbell and with regular DFT for the OOTV configuration are not given, as both configurations relaxed into the Type B tetrahedral during energy minimization. The structure is defined in Figure 5-1. A schematic of the OOTV configuration could be seen in Figure 5-4.

From our DFT calculations, we find that the octahedral vacancy type is significantly more energetically favorable than the tetrahedral vacancy type. The different interstitial types are in contrast quite energetically competitive. However, we note that the

---

[*] From quantum mechanics, one can at most obtain a charge density for the "location" of the electrons in a system. There is no exact method to divide up this charge density into zones belonging to each atom for the purpose of counting the number of electrons each atom has.

deepest energy minima we found for the interstitials for both regular DFT and DFT+U are not the "expected", conventional interstitial defect types (i.e. Type B tetrahedral, Type C tetrahedral, octahedral). Regular DFT favors the formation of a defect dumbbell in a normally occupied octahedral site, while DFT+U favors the displacement of an tetrahedral atom from its regular lattice site to form a complex consisting of two octahedral interstitials and one tetrahedral vacancy which we term the OOTV complex (Figure 5-4). Neither of these defect types, which are of a delocalized form in comparison to the conventional site-specific defects, is, as far as we know, reported in the literature.
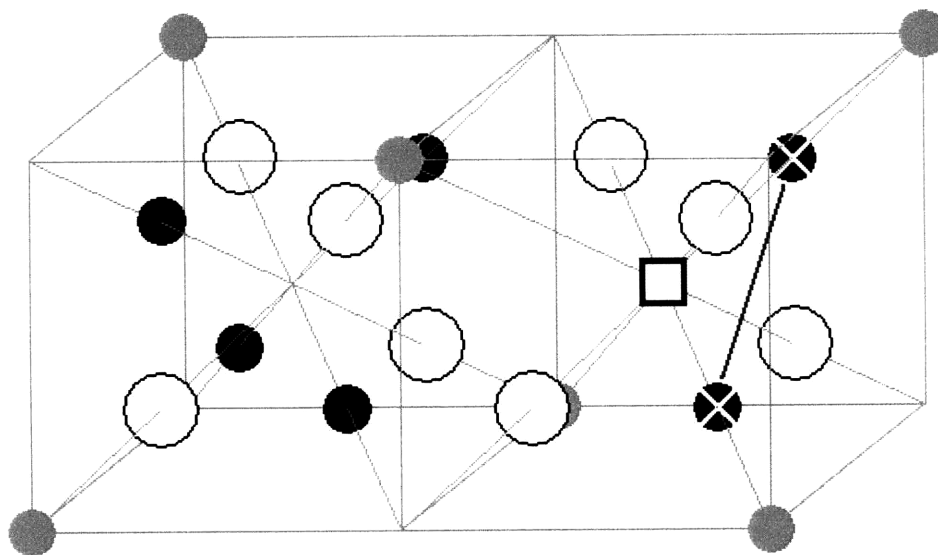
Figure 5-4: The octahedral-octehedral-tetrahedral vacancy (OOTV) interstitial defect configuration is formed around a tetrahedral vacancy (square) adjacent to two octahedral interstitials (black with diagonal cross). A dark gray line marks the "axis" of the defect. The OOTV configuration could be thought of as the midpoint of interstitialcy diffusion mechanism 2 (following the standard notation [86], see Figure 5-5).

We note that for all defect species, the magnitude of the entropy of formation is roughly equal to 1/3 that of the formation reaction of Fe_3O_4[*]. That all these formation entropies are nearly equal in magnitude is a result of the dominance of the entropic changes by the confinement into or release from oxide of free O_2 molecules (in

---

[*] Note that all the defect formation reactions form or consume 1/3 of a formula unit of Fe_3O_4 at the sites of repeatable growth.

comparison to the differences in vibrational properties between the condensed phase configurations, with or without defects). We also note in passing that the regular DFT energetic results (including those of the migration discussed later and presented in Table 5.2) are compatible with those computed earlier by Hendy *et al.* [85]. However, it must be pointed out that this earlier work neglected to sufficiently explore the energy landscape, missing, for instance, the Type B interstitial position, perhaps due to the overaggressive use of symmetry in the supercell calculation.

5.2.2 Diffusion Mechanisms

Calculated activation energies for select defect migration paths and reactions from one defect type to another are summarized in Table 5.2.

Defect Migration Pathway			Regular DFT [eV]	DFT+U [eV]
Fe Vacancy	Octahedral	3	0.88	0.76
Fe Vacancy	Tetrahedral	1	0.94	0.84
Fe Vacancy	Oct. → Tet.	N/A	2.66	3.54
Fe Interstitialcy	Oct. Dumbbell → Oct. Dumbbell	N/A	0.19	N/A
Fe Interstitialcy	OOTV. → Tet. B	N/A		1.23
Fe Interstitialcy	Oct. → Oct.	4		1.07
Fe Interstitialcy	Oct. → Oct.	5		0.73
Fe Interstitialcy	Oct. → Oct.	6		1.69
Fe Interstitialcy	Tet. B → Tet. B	9		0.92

Table 5.2: Activation energies for defect migration and transitions calculated with and without the +U formalism. Numbers are provided for pathways that are found in the standard catalogue [86]; the interstitialcy pathways are depicted in Figure 5-5. No comparison is provided with pathways 7 and 8 as they do not contribute to diffusion. The OOTV → Tet. B migration pathway can be compared to pathway 2. This is because the OOTV configuration (Figure 5-4) can be thought of as the midpoint of pathway 2.

For both sets of calculations, the transition-state energies for vacancy migration are roughly in agreement. Both give a comparatively lower energy and the same atomistic pathway for the octahedral vacancy migration. The two methods differ in the interstitial diffusion results. Regular DFT yields a near negligible migration energy for the octahedral dumbbell, its most favored energetic defect configuration. DFT+U gives a significantly larger barrier, 1.23 eV, for the most energetically favorable interstitial defect type.
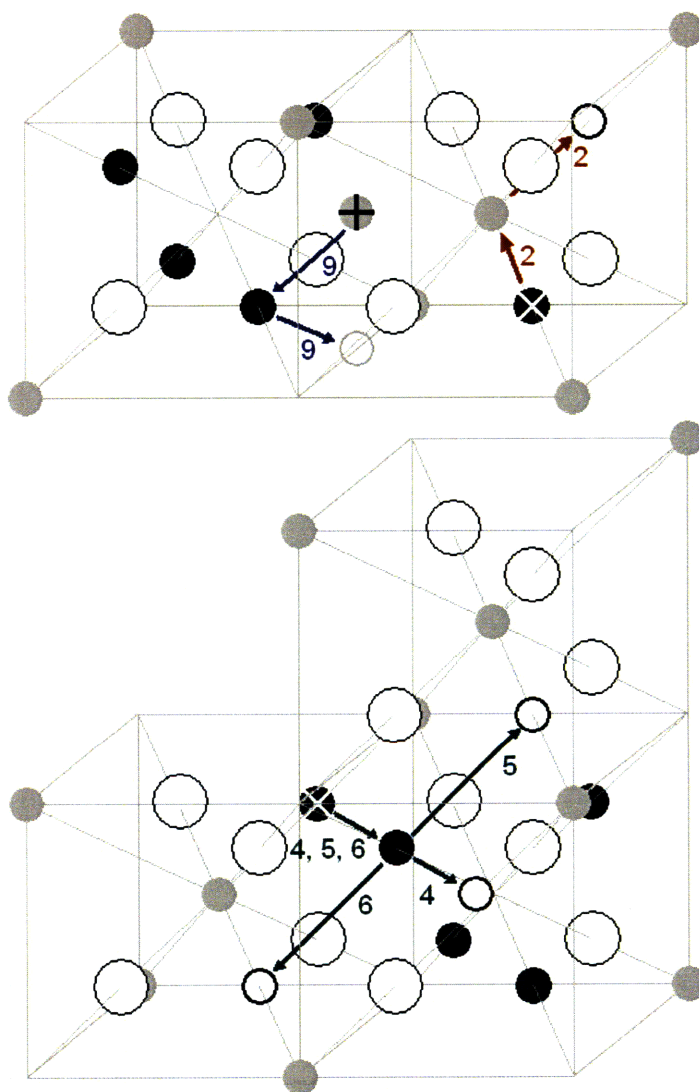
Figure 5-5: Various interstitialcy diffusion pathways in $Fe_{3-\delta}O_4$. The component moves of each jump are designated by the numbers it is designated in [86].

5.3 Diffusivity in $Fe_{3-\delta}O_4$: Experiments and Atomistic Calculations

Cation transport in nonstoichiometric $Fe_{3-\delta}O_4$ is experimentally known to occur via the vacancy mechanism as well as interstitialcy mechanisms [86]. For the vacancies, the experimental findings, some of which have been mentioned in Section 5.3.1 and 5.3.2, can be summarized as follows:

1. The octahedral vacancy appears to be the dominant vacancy type [97].

2. Defect formation energy equilibrium constants have been created from fits to experimental nonstoichiometry result [19]. The Gibbs free energy of formation of the more energetically favorable vacancy type can be obtained from these fits as
$$-2.34 eV + 0.00133 \frac{eV}{K} T .$$

3. There is no non-Arrhenius temperature dependence of the equilibrium constant of vacancy formation [19].

4. The measured activation energy of vacancy diffusion is 0.90 eV, which permits an interpolation of activation energies of 0.76 eV and 1.26 eV for the octahedral and tetrahedral vacancies respectively if a small fraction of the vacancies are assumed to be tetrahedral [20].

Our calculations of the vacancy formation energetics indicate that the octahedral vacancy is significantly more favorable than the tetrahedral vacancies (an energy difference of 1.89 eV for regular DFT and 1.11 eV for DFT+U). This agrees with the first observation. The calculated results of the formation energy and entropy of the octahedral vacancy, as seen in Table 5.1, match well with observation 2. We do note though that in comparison to the experiments, the energetics calculated with DFT for both vacancies and interstitials

are systematically biased towards oxidation[*]. The source of this discrepancy is unknown, but perhaps the correction of -1.36 eV per O_2 molecule developed for pure solid formation calculations [92] might not be appropriate for defect formation calculations. Our finding, as discussed in Section 5.3.1, that the formation entropies are roughly equal for both vacancy types means that at no temperature is the Gibbs free energy of formation of the tetrahedral vacancy equal or lower than that of the octahedral vacancy. As this would imply that at no temperature is the tetrahedral vacancy dominant in number over the octahedral vacancy, we expect that the experimental measurements would always measure the property of only one defect type and would not yield a non-Arrhenius behavior, consistent with observation 3. Our results for the vacancy migration activation energies, as seen in Table 5.2, match well with observation 4. In sum, we find good agreement between the experimental findings and the calculations from DFT.

The interstitials present a more complicated case for analysis. The essential experimental findings for the interstitial are as follows:

A. From the fits to experimental nonstoichiometry result [19], a ΔG of $4.17eV - 0.00103\dfrac{eV}{K}T$ has been obtained for defects dominant in number below 1573 K and a ΔG of $7.47eV - 0.00308\dfrac{eV}{K}T$ for defects dominant in number above 1573 K.

B. Interstitials migrate by interstitialcy mechanisms, not direct jumps [86].

C. The interstitial type numerically dominant at low temperatures is found to have an activation migration energy of 2.37 eV [20]. The interstitial type numerically dominant at high temperature is found to be virtually immobile.

---

[*] That is, the energies of formation from DFT compared to experiments are higher for interstitials and lower for vacancies. Oxygen is a byproduct of interstitial formation while it is a reactant in vacancy formation.

D. From the analysis of the correlation factors [20], two interstitialcy mechanisms appear to be operative for the mobile defects. At temperatures lower than 1323 K, the dominant mechanism is of an unknown type not found in the standard catalogue [86]. At higher temperatures, the dominant mechanism has a correlation factor closest to that of mechanism 9 [86].

With the bias of the DFT formation energies towards oxidation as discussed previously, it is difficult to compare the calculated results with the experimental results when, as seen in Table 5.1, DFT yields so many energetically-competitive interstitial types. However, it is instructive to compare the formation entropies. We obtain a value for all our calculated defect types roughly equal to the experimental measurement of the low-temperature defect. For the defect type dominant in number at high temperatures, the magnitude of the formation entropy is three times larger. This means that the formation entropy of this defect can no longer be attributed to the release of 2/3 free O_2 molecules for the formation of one defect as discussed in Section 5.3.1. One possibility for the difference is a drastic change in the material vibration properties caused by the formation of this defect of unknown atomic configuration. Another (likelier) possibility is that these high-temperature interstitials are formed through an entirely different and unknown defect formation reaction as those considered in Section 5.2. Indeed, the measured formation entropy of this defect type is nearly exactly 3 times larger than the formation entropy of the defect reactions. This suggests the possibility that 2 O_2 molecules are freed as products of the formation of one of these defects (which in this case would not be an interstitial but rather a defect cluster). In turn, this would match well with observation C that these defects are virtually immobile.

DFT also indicates the possibility that the most energetically favorable defect types need not be of the conventional octahedral or tetrahedral interstitial configurations.

Configurations favored by DFT, such as the OOTV type seen in Figure 5-4, can provide an explanation for observation B, in that these defects, which are delocalized in comparison with the traditional defect types, would obviously not migrate by the direct interstitial jump mechanisms. They could also account for observation D, in that these defect types would not migrate by interstitialcy mechanisms of the conventional defect types as catalogued in [86].

Observation C presents some troubling issues for the atomistic calculations. The regular DFT result is simply far too low compared with the experimental value to be considered physical. We find that regular DFT is unsuitable for simulations of $Fe_{3-\delta}O_4$. It appears that the conclusions drawn in earlier works [85], where the authors did not systematically explore the interstitial diffusion, might be a result of the fortuitous ability of regular DFT to provide reasonable results for the vacancy diffusion, rather than its actual ability to model $Fe_{3-\delta}O_4$. The DFT+U result is more reasonable, but is still too low in comparison with the experimental result. A possible cause might be a deficiency of the +U formalism in terms of modeling atomic configurations with point defects. Alternatively, it might be that a more extensive exploration of the energy landscape than the one conducted in this study is needed to find more energetically favorable defect configurations of a similar delocalized nature and their associated diffusion pathways. As it stands, based on the current results we can make no firm conclusions about the specific configuration of the most favorable interstitial defect configuration and the specific diffusion pathway it takes. We could only conclude that future studies of interstitial diffusion in $Fe_{3-\delta}O_4$ must consider defect types not of the traditional localized form. However, the computational cost associated with DFT renders the sort of massive energy minima search needed for this task impractical at present.

6   Creep in Nanocrystalline Fe

6.1   State of Understanding and of Computer Simulations

Creep is the inelastic deformation of material under a constant applied load. As some sort of diffusional process (which typically has a significant energy barrier) is involved, creep is a slow dynamics phenomenon. In general, creep rates can be expressed as proportional to some diffusion constant and some power of the stress [10]

$$\dot{\varepsilon} \propto D\sigma^m$$

Both D and m are properties of the dominant creep mechanism at work, which usually derives from the microstructure. Diffusivities in the lattice in comparison to that in the grain boundaries typically have a higher energetic barrier and thus occurs more slowly; but creep mechanisms involving lattice diffusion such as vacancy-driven dislocation climb (discussed in Chapters 3 and 4) are in most cases predominant due to the much higher volume fraction of the bulk lattice versus grain boundaries in the typical material. In contrast, in the case of nanocrystals, where the grain boundaries become a significant portion of the microstructure [15], the smaller barriers to the grain-boundary diffusion mechanisms allows the grain-boundary mechanisms to predominate.

In the cases where grain-boundary mechanisms dominate the creep phenomenon, the observable deformation of creep is a result of the sliding of grains versus each other. This grain-boundary sliding can be categorized into two types [98]. Rachinger [99] (or "primary" [2]) grain-boundary sliding is an independent creep deformation mechanism (thought to be responsible for superplastic flow [98]) and is identified by a strain rate proportional to the square of the applied stress [2, 98]. Lifshitz [100] (or "secondary" [2])

grain-boundary sliding is not an independent creep deformation mechanism, but rather a non rate-controlling process that accommodates other diffusional creep mechanisms (e.g. Coble, Nabarro-Herring) and is geometrically necessary for maintaining grain compatibility. (Both Coble and Nabarro-Herring creep are identified by a strain rate proportional to the applied stress [10] and thus the Lifshitz mechanism is readily contrasted with the Rachinger mechanism.) Despite theoretical attempts to justify these trends (e.g. [101] for the Rachinger mechanism), the essential understanding of how the atoms move within the grain boundaries and of how these nanoscale processes contribute to the observed macroscopic deformation is missing.

One approach taken to investigating the issue with atomistic technique was to directly simulate the actual deformation of nanocrystals with MD, but with extreme strain rates to compensate, in a brute-force fashion, for the method's inability discussed in Chapter 1 to investigate long-timescale problems. (The energetic barriers to the creep deformation that cause the slow dynamics are variously overcome by extreme temperature [17], extreme applied stress [16], or extreme applied strain [102] in the simulations, resulting in high strain rates of 10^7-10^{11} s^{-1}.) The fundamental question with the approach[*] is whether creep is actually even simulated at all, if the material lengthens by a billion times within one second. However, even suspending such disbelief, the difficulties associated with forcing slow processes to happen quickly is summarized in one such study [102],

> One of the rationales using a ... zero-temperature simulation ... to study
> the deformations was the hope that the system would evolve through a
> series of local energy minima, separated by discrete events when the
> applied deformation causes the minima to disappear. In this way, the

---

[*] The passage by Nabarro [2] quoted in Chapter 1 is a statement of such skepticism.

simulation would have resulted in a unique deformation history for any given sample. However, the deformation turned out to happen through a very large number of very small processes, that could not be individually resolved by this procedure. One symptom of this is that the individual [calculated stress-strain] curves are not completely reproducible. Any even minor change in the minimization procedure, or a perturbation of the atomic coordinates, will result in a slightly different path through configuration space ....

The inability to isolate each unit process due to the high strain rate in these simulations means that the unit processes cannot be correlated to the overall deformation in all but the most qualitative sense. However, these atomistic investigations do demonstrate the value of simulations in this area as they are able to duplicate quantities measureable in experiments (e.g. strain rate versus stress curves [17]) and replicate some features of the creep processes (e.g. the Lifshitz mechanism [17]).

A second approach is to first simplify the boundary to highly ideal but very well characterized structures [103], and then study the possible transitions in high-symmetry bicrystals with these boundaries using atomistic techniques such as molecular statics [104] or NEB [105]. Such studies can give detailed atomistic and energetic information of grain-boundary sliding. However, these simulations all require strict assumptions about how the material deforms, and as such the ability to capture the dynamic evolution of the boundary during creep is lost. The idealization of the boundaries to abstract structures also has the possibility of removing much of the essential physics that arises out of the disorder of the boundary, where liquid-like diffusion mechanisms are found to operate [106].

6.2 An Alternate Approach to Creep

We aim to use atomistic simulations to attribute the atomic unit processes with the actual deformation in order to understand the long-timescale creep processes. To that end, we need an actual trajectory of deformation at realistic strain rates where unit processes can operate and be studied in isolation.

Noting the merit of the overall scheme of the MD studies discussed in the previous section [102, 16, 17], we adopt the same approach of directly simulating the deformation of the material under an applied stress. However, instead of using MD to explore the energy landscape, we employ the novel ABC method described in Section 2.3.2. The method is capable of providing a trajectory of the deformation in the sequence of individual unit processes without the need for an artificial load (e.g. extreme temperature) and is therefore ideally suited for the problem.

For the sake of consistency with the other discussions within this thesis, we study Fe nanocrystals and employ the same Finnis-Sinclair empirical potential for Fe discussed in Chapter 3 as the energy landscape. We consider 2 models of grain structure, a 3-D system of spherical grains arranged in a BCC array[*] and a 2-D system of columnar grains arranged in a close packed lattice. To form the model system, a slow cool was conducted with MD on a melt with small seeds of Fe atoms[†] at the desired centers of the grains. The spherical grain system consists of 2 (nearly completely) spherical grains, each 29.8 Å in diameter unstrained with 3456 atoms in total. The columnar grain consists of 4 grains in an unstrained overall box size of $39.0 \times 39.0 \times 19.1$ Å containing 2408 atoms, with the

---

[*] It is necessary to arrange the grains in some lattice to fit with the use of the periodic boundary condition. The array which yields the most nearest neighbors for every grain would most closely approximate a spherical grain. Although the FCC array is better than BCC in this regard, we use the BCC array in order to generate bigger grains for the same number of atoms. This is because in an orthogonal simulation cell, the minimum number of grains needed for the BCC array is 2 while that of FCC is 4.

[†] The grains of BCC atoms are randomly oriented versus one another.

columns oriented along the short axis. A snapshot of the atomic configurations can be seen in Figure 6-1.
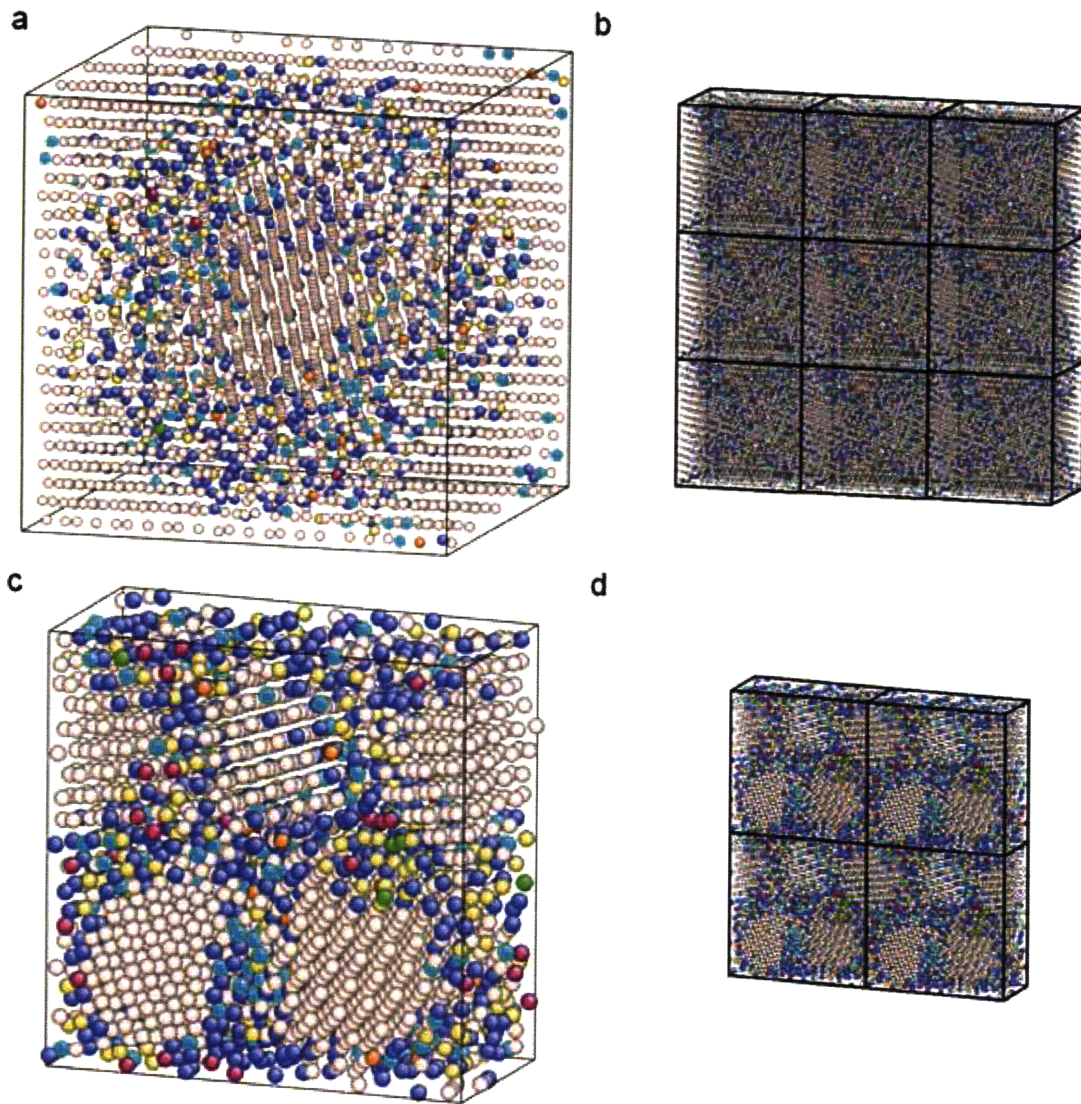
Figure 6-1: The model systems of spherical and columnar grains. (a) Snapshot of the atoms within the simulation cell, which contains 2 spherical grains of BCC Fe, randomly oriented versus each other. The grains themselves are positioned in a BCC array within the simulation cell. (b) The simulation cell of the spherical grains in the context of the periodic boundary condition. (c) Snapshot of the atoms within the simulation cell, which contains 4 columnar grains arranged in a close packed 2D lattice. (d) The simulation cell of the columnar grains in the context of the periodic boundary condition. The atomic configurations are colored by coordination, where darker atoms indicate imperfect coordination and could be used as a rough guide for visualizing the grain boundaries. Figure generated with Atomeye [78].

From ABC, we obtain a trajectory of consecutive energy minima and the energy saddle points in between. We estimate the time required for each activation process using transition-state theory [5]

$$t_{A \to B} = \left(\nu_\circ \exp\left(-\frac{\Delta U_{A \to B}}{k_B T} \right) \right)^{-1}$$

where ΔU refers to the activation energy obtained for each unit process. This permits us to obtain the overall rate from the unit processes by dividing the observed deformation by the total time for all the component unit processes.

6.3   Findings

6.3.1   Energy Evolution

From our transition-state pathway trajectories, we find that the energy evolution during the creep deformation takes the form of a series of "saw-tooth" oscillations punctuated by sudden energy relaxations. Some calculated results, accompanied with a schematic that identifies some of the features, can be seen in Figure 6-2. From the energetic point of view, each individual saw-tooth is a minor transition that appears to be reversible, namely, that the minima before and after have roughly the same height. (We find that the associated barrier is somewhat variable, but, notably, is independent of stress. For the spherical model, this value hovers around between 0.4 eV to 0.6 eV. For the columnar grains, the barrier is generally between 0.6 eV to 1.2 eV. It should be noted that variable barriers are also observed in experimental measurements of stress relaxation on nanocrystalline Fe [107].) The energy drops in between a series of saw-teeth, however, make the relaxations kinetically very difficult to reverse. This is because the significant difference in the relative heights of the minima means that the forward barrier is much

larger than backward barrier. (The net energy drop is extremely variable and it seems perilous to set a bound. Nonetheless, from our calculations, we find that the drop could be relatively small at about 0.6 eV to more than 2 eV.)

The influence of stress on these features is also visible in Figure 6-2(a). Firstly, we find that at higher stresses, the drops in energies due to the collective motion are significantly larger. This is understandable from the fact that the energetic penalty for "backwards" microstructural evolution during creep should be higher at higher stresses. Secondly, the number of saw-tooth oscillations in between the relaxations falls. This is best understood from the point of view of the atomic processes, which we discuss in detail in the following section.
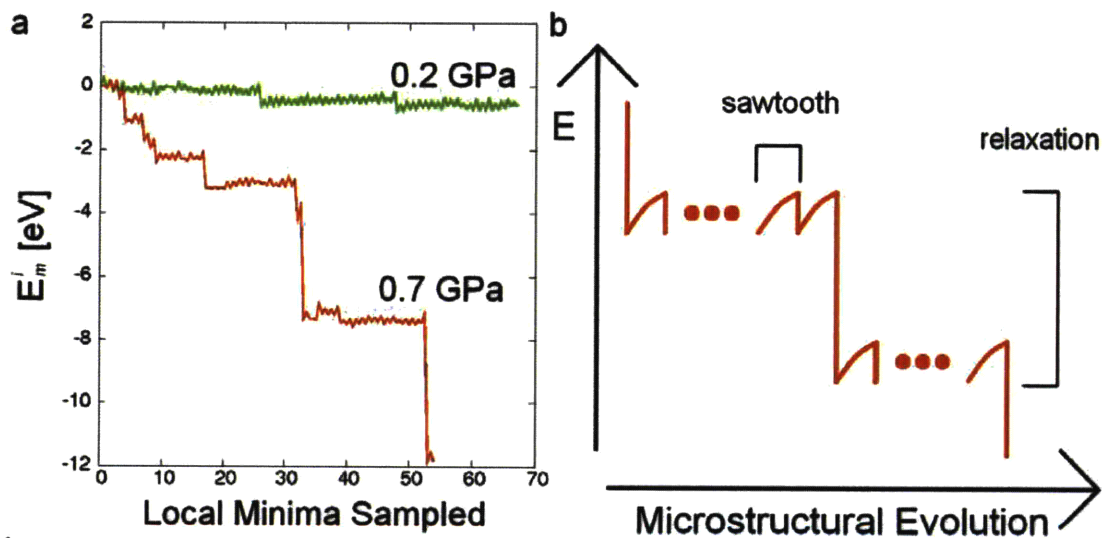
Figure 6-2: (a) Results of the energy evolution of the simulated creep trajectories for the spherical grains, at 0.2 GPa and 0.7 GPa. (b) Schematic of the energy evolution during the creep of nanograins, illustrating the key features. We find that the trajectory follows through a series of energy saw-tooth oscillations in between sharp energy relaxations. These features are general for both the spherical and columnar grains.

Figure 6-3 shows the atomistic mechanisms that one can deduce from the atomic configurations at various points along the generated trajectory. Inspection of the atomic configurations associated with the energy minima on each side of a saw-tooth indicates "minor", local rearrangements within the grain. An example of this type of displacements is seen in Figure 6-3(a). Inspection of the atomic configurations immediately after each sudden energy relaxation indicates coordinated atomic motions that could be regarded as an extended interstitialcy mechanism which results in the injection of atoms into the grain boundary, as seen in Figure 6-3(b). This also can be interpreted as an incorporation of atoms from the grain boundary into the grain leading to a form of grain growth.
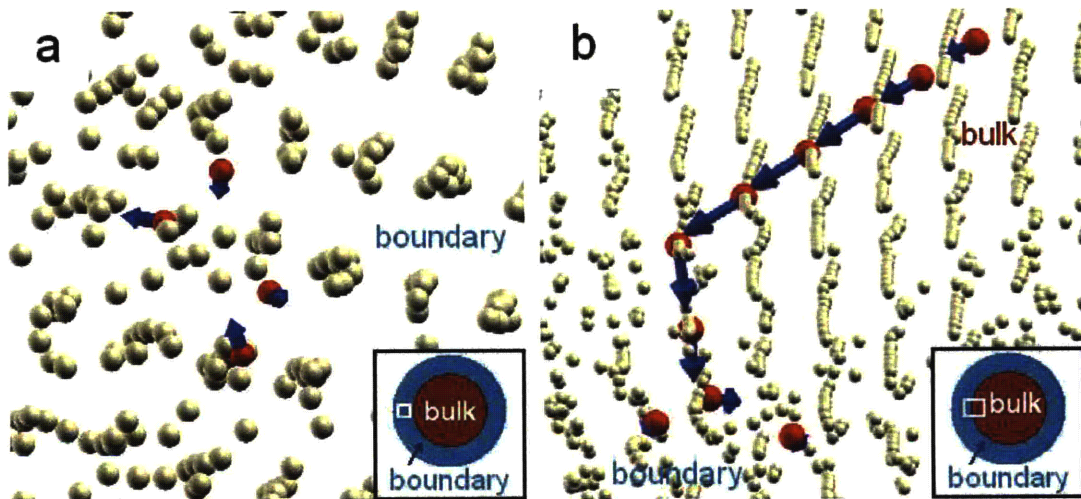
Figure 6-3: Atomic displacements during creep for the spherical grain at 0.2 GPa. The features are general for both spherical and columnar grains. (a) Localized grain-boundary response, obtained from a comparison of 2 atomic configurations separated by an energy saw-tooth. (b) Injection of an interstitial atom into the grain boundary by the collective displacements of atoms along $\langle 111 \rangle$ direction which is the nearest neighbour direction in the BCC lattice, obtained from a comparison of 2 atomic configurations at the end of two successive energy drops (i.e. separated by a series of saw-tooth oscillations and one energy drop). Atoms that have displaced more than 0.1 Å or more are marked in red/dark shade. The arrows mark the direction and relative magnitude of atomic displacements. Each inset shows the enlarged area (small rectangle) relative to the bulk (spherical grain) and surrounding boundary in each case. Thus displacements in (a) occur entirely in the boundary, whereas displacements in (b) start in the grain (bulk) and end up in the boundary region. Figure generated with XCrysDen [108].

From an atomistic standpoint, we find then that the atomistic precursors to creep in the conventional sense consist of a series of localized "adjustments" in the grain boundary, manifesting as a saw-tooth behavior in the energy trajectory. These rearrangements then enable the coordinated displacements that lead to the removal or addition of atoms in the grain which in turn result in changing the grain shapes, which are associated with sharp drops in the energy as the microstructure evolves and which are irreversible. That variability as observed in the associated energetics discussed in the previous section is thus unsurprising as these atomic motions have a great dependence on the local environment and so the energy barrier of the transition should be expected to reflect the random nature of the grain-boundary structure.
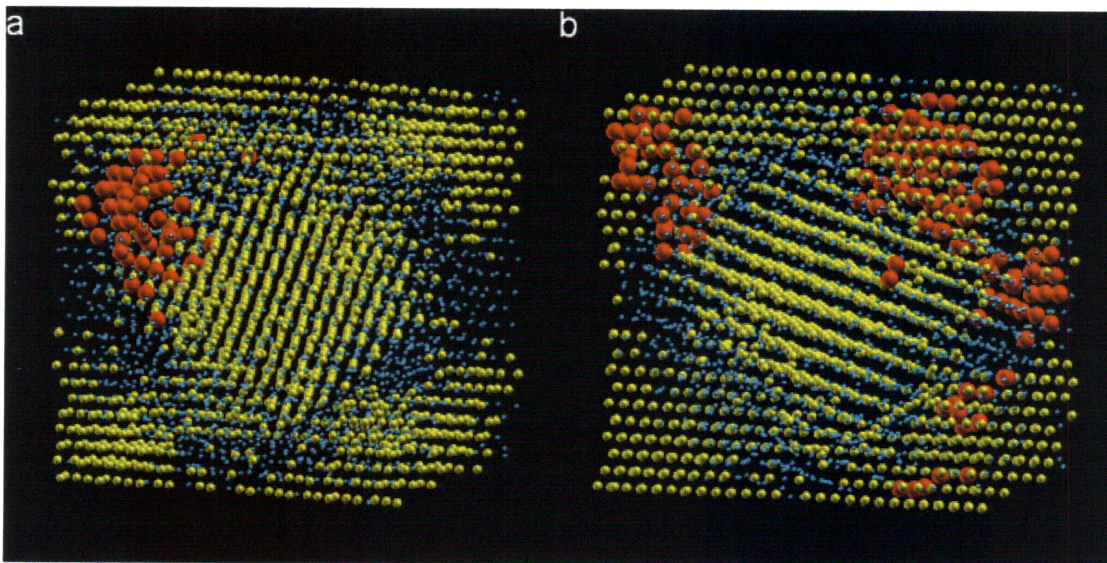
Figure 6-4: A comparison of the extent of atomic movement in the spherical grains. (a) The atomic movements at 0.2 GPa, obtained from a comparison of 2 atomic configurations between two successive energy relaxations. (b) The same for 0.7 GPa. Bulk atoms are colored yellow, atoms near the grain boundary are colored blue, and atoms that have displaced more than 0.1 Å or more are marked in red. Figure generated with XCrysDen [108].

While stress does not appear to change the character of these individual transitions, it has a general effect on the extent of these motions throughout the material. Figure 6-4 illustrates the atomic processes that occur during the energy saw-tooth

oscillations in the context of the whole grain between two sharp energy drops for two different stress loadings. We find that at the higher stress the number of sites which registered motion is much more widely distributed throughout the whole material. Combined with the previous observation that stress does not significantly change the barrier height of the energy saw-tooth, that is, beyond the normal variability of the associated barriers, we conclude that stress has the effect of lowering the barriers of localized adjustments at some sites. Thus at higher stresses, adjustments are competitive at more sites around the grain boundaries, which result in the observation of more atomic motion throughout the material. The observed fall in the number of saw-tooth oscillations between sharp relaxations at higher stresses can be understood to be the consequence of this more efficient probing of "weak spots" around the entire material.

From this point of view, we can understand the problem with using extreme loading to overcome the deficiency of MD with respect to the timescale. When an extreme load is used (be it large stress, large strain, or large temperature), more atomic transitions are simultaneously activated around the material and so more atoms are in motion. That the authors of the study [102] quoted in Section 6.1 have trouble resolving individual processes even when using 0 K simulations can be attributed to this effect.

6.3.3   Direct Rate Calculation

The process of calculating the rate of creep deformation is illustrated in Figure 6-5. We begin with identifying the energy minima along the entire trajectory. Then we use the energy barriers between the minima to calculate the time between each transition, which correlated with the known strain deformation at each minimum, permits the calculation of strain as a function of time.
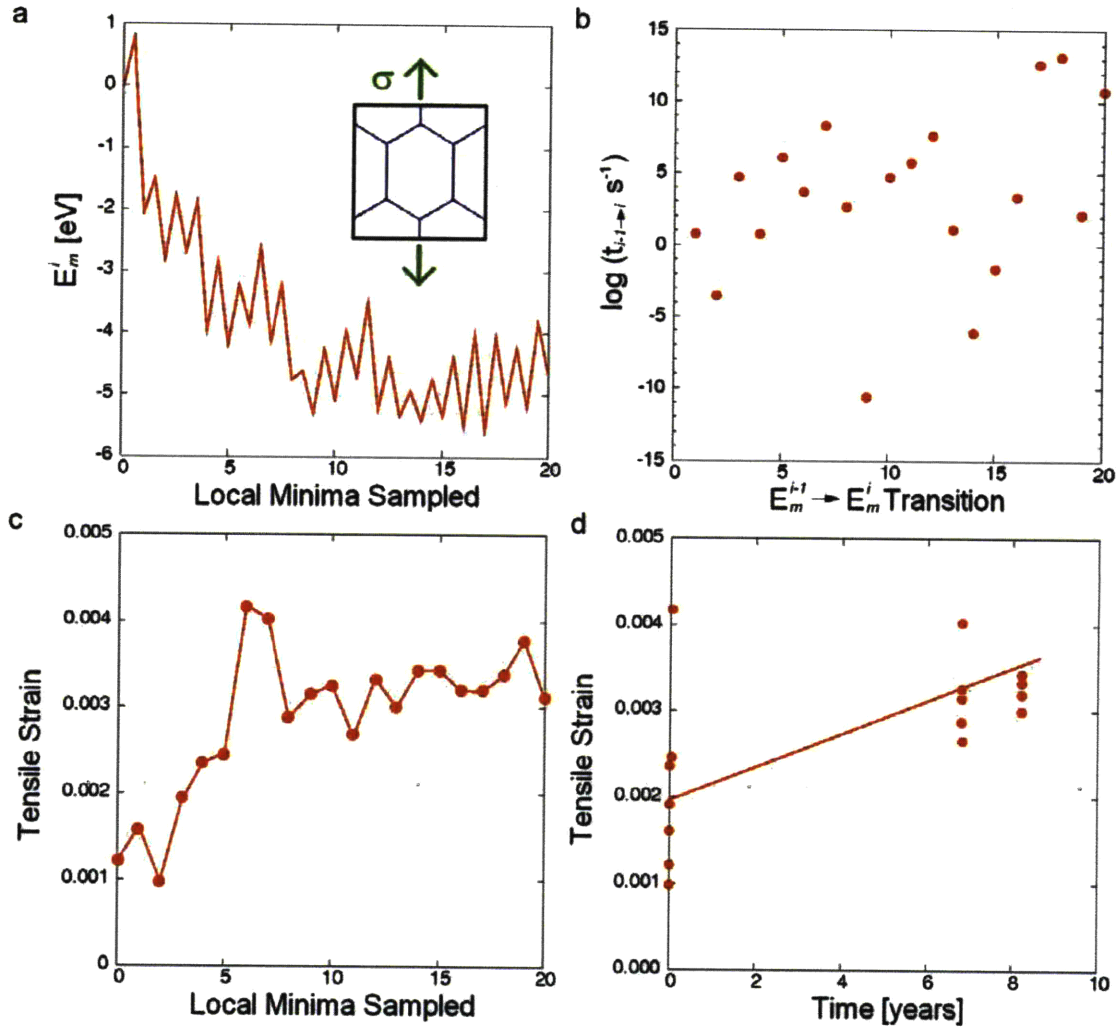
Figure 6-5: The strain rate of the columnar grain system at 0.2 GPa and 300 K. (a) We begin with the energy of transition between the energy minima as we sample the energy landscape. (b) Using the rate equation and an assumed frequency factor ν of 10 THz, we are able to obtain the time of transition between each minimum. (c) The strain calculated from the cell dimension of the atomic configuration for each energy minimum. (d) Combining the time information (b) with the cell dimensions of the atomic configurations at the different minima (c), we obtain a plot of the strain as a function of time. Fitting a line to (d) yields the strain rate of $0.52 \times 10^{-11} \, s^{-1}$.

Figure 6-5(d), a result from the columnar grain, shows the general trend that the deformations sampled undergo "fast" transitions (too rapid to resolve on the scale of this figure), except for two slower events, both on the scale of years. Within any short time interval the data are too scattered to reveal any trend. However, on the long time scale

(years) an overall positive trend leads to a strain rate of the order of magnitude mentioned by Nabarro [2].

The corresponding plot of the strain of the spherical grains (created from the energy trajectory seen in Figure 6-2) is given in Figure 6-6, which likewise demonstrates the tendency for "fast" transitions to be punctuated by a few slower events. We notice that the strain rate for the spherical grains is much higher than that of the columnar grains. This is a direct consequence of the lower energy barriers observed for the spherical grain discussed in Section 6.3.1.
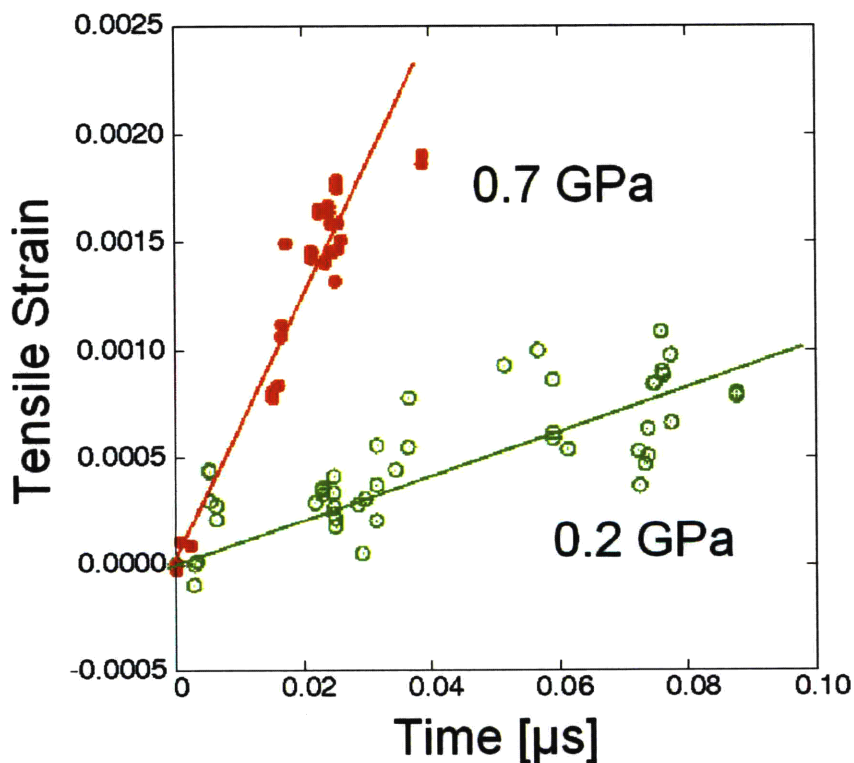
Figure 6-6: The strain as a function of time for the spherical grain stressed at 0.2 GPa and 0.7 GPa at 300K. These curves correspond to the energy trajectories seen in Figure 6-2. From fits to the plots we obtain estimates of strain rate of 1×10^4 s^{-1} at 0.2 GPa and 7×10^4 s^{-1} at 0.7 GPa.

6.4   Summary

We have described an attempt to replace molecular dynamics simulation by a method based on activated state kinetics in the study the atomistic aspects of structural deformation in condensed matter, motivated by the desire to reach longer time scales. This autonomous basin climbing method thus far has allowed us to tackle the longstanding problem of computing, using interatomic potentials, the temperature dependence of shear relaxation in supercooled liquids, with implications for understanding the nature of glass transition. When this approach is extended to the response of nanostructures, in the form of 2-D columnar and 3-D spherical grains under tensile loading, we find the results sensitive to the structural characteristics of each system in ways that are rather reasonable. We have successfully used the method to approach a strain rate many orders of magnitude slower than was previously achieved in MD simulations, and in doing so successfully identified the atomic processes which contribute to the macroscopic strain.

7 Retrospect and Prospect – Obtaining Rate from Computation Studies

In this thesis, we used computational techniques to investigate four problems of rate in creep and oxidation, each discussed in a separate chapter. These all belong to the general class of slow dynamics microstructural evolution problems, which could not be studied with traditional atomistic simulation methods like molecular dynamics. To attack the problems, we took the same general strategy, in that we broke down the overall deformation into component transitions and then constructed understanding of the rate of deformation from these transitions using concepts of transition-state theory. However, as a result of the differences of the environment in each of the problems, in terms of system properties such as chemistry and level of symmetry, the pathways of deformation have their own unique characteristics, which must be taken into account during the development of the solution strategy. As a result, despite the similarities of the problems and general methodology, different techniques were employed to obtain the rate information for the four problems.

Through our investigations, we learn that there are three key properties of the unit processes that govern how we approach each problem. The first is whether these transitions are predictable or not. The systems we investigate are all solids, and we generally find that they involve well defined lattices with a high level of symmetry. In these cases, while the pathways might be complicated and tedious to compile, such as the 1Va-2C transitions discussed in Chapter 3, with sufficient diligence one can generally succeed in identifying them by searching through all the possible nearest neighbor jumps on the defect sublattice for some arbitrary starting defect configuration. The exception within the four problems is the study on nanocrystalline Fe in Chapter 6. Due to the

highly disordered atomic structure in the grain boundary, it is impossible to construct a full and complete list of plausible atomic jumps from a starting configuration. The predictability of the pathways is essential in terms of the choice of the method used for transition-state search. NEB has an intrinsic appeal in its simplicity and ease of implementation. As discussed in Section 2.3.2, however, it requires the input of a final state configuration in addition to the initial state configuration. If the complexity of the microstructure is such that no guess can be ventured for the final state, then the method is simply not applicable. As such, NEB has been used with success in the bulk of the problems in this thesis, where the microstructure is sufficiently "simple" that the pathways are predictable; ABC, which requires no guessing for the transitions, is employed for use in the problem of nanocrystalline creep where the liquid-like structure of the grain boundaries makes guessing pathways unfeasible.

A second property of the unit processes we have found that governs our approach is the number of unique, plausible pathways in the system. In a crystal with translational symmetry, transitions could generally be mapped onto one another to keep the number of calculations needed to obtain pathways under control. However, in the presence of some symmetry breaker, the number of unique pathways that emerges could become potentially infinite in number. We discover this character in two of the problems in this thesis. In our calculation of vacancy diffusion barriers as part of the calculation of the dislocation climb rate in Chapter 4, the presence of the dislocation removes the symmetry of the lattice and renders all barriers of all diffusion moves which are not parallel to the dislocation line unique. In the problem of creep in nanocrystalline Fe, the disorder in the grain boundary makes the number of plausible diffusion jumps infinite. This has two consequences, the first of which is in terms of selecting a method to search for transition-states. When one uses NEB to derive rate information, one is essentially taking the approach of calculating rate from a catalogue of barriers. This approach is obviously

futile when the number of plausible barriers is infinite, and calculating rate from a system evolution trajectory, as one would when one uses ABC, is a far more manageable approach. In the dislocation study, we were able to keep the barrier calculations under control by using elasticity theory and literature results [70] as a guide to successfully simplify the trends. In the Fe nanograin study, we do not have the benefit of reducing the barrier calculations and we find yet another compelling reason to use the method of ABC for obtaining a trajectory through the energy landscape. The second consequence of the number of barriers lies in the choice of method used to calculate the rate from the barriers. This is most obvious when we compare our approach to the problem of bulk diffusion in carbon-supersaturated Fe described in Chapter 3 and to the problem of vacancy dislocation interaction described in Chapter 4. In the study of Va-C clusters, we are able to isolate the relevant unit processes that contribute to the overall rate to two, the vacancies and the divacancies jumps. This is a very manageable number that leads to the simple, yet successful, analytical treatment described in Section 3.5. However, the number of barriers in the dislocation study was such that numerical integration over the pathways is necessary. The task of calculating rate becomes much more complex and difficult.

Phenomenon Investigated	Properties of Atomistic Unit Processes			Problem Solution Strategy	
	Are Pathways Predictable?	Are Unique Pathways Potentially Infinite?	Are Details Experimentally Available?	Obtaining Unit Processes	Understanding Rate from Unit Processes
Bulk Diffusion in BCC Fe Supersaturated in C	Yes	No	No	NEB	Analytical, from Barriers
Dislocation Climb Velocity in BCC Fe	Yes	Yes	No	NEB	Numerical Integration (kMC), from Barriers
Diffusion in Nonstoichiometric $Fe_{3-\delta}O_4$	Yes	No	Yes	NEB	Interpretation of Experiments Informed with Atomistic Calculations
Creep in Nanocrystalline Fe	No	Yes	No	ABC	Analytical, from Trajectory

Table 7.1: Summary of details and approach taken towards the four investigations in this thesis.

The third property of the unit processes that had an effect on how we approach the four problems is the availability of experimental information. Experiments on the rate of microstructural evolution are rarely able to provide the level of detail of the atomic processes to permit detailed cross-comparisons with that obtained from calculations. This is because experimental techniques are generally capable only of measuring integral properties and are unable to distinguish between different competitive mechanisms and measure their respective contribution to the overall material deformation. This means that the rate trends we obtain from our calculations could only be compared to experimental rate trends, as is done in the study on the Va-C point defect clusters discussed in Chapter 3. The study of diffusion in nonstoichiometric $Fe_{3-\delta}O_4$ spinel proves to be the sole exception. While experiments cannot explain all the possible trends, some experimental details and inferences of the atomic unit processes do exist [19, 20]. In this unique case we are able to integrate our calculations with the experimental results to create a richer, more scientifically satisfying understanding of the rate.

A summary of these properties of the unit processes in each of the component studies of the thesis as well as the approach taken to calculate rate is provided in Table 7.1. As can be seen, these problems address different areas within the overall theme of slow dynamics problems and as such are complementary.

Nonetheless, despite the wide range that these problems cover, we must admit that they do not span the full spectrum of the class of slow dynamics problems and that the solution strategies we employed therefore cannot be used as a template for every conceivable slow dynamics problem. We could find one such example by examining the foundation of success of our solution strategy for the problem of creep in Fe nanocrystals. As discussed in Section 2.3.2, ABC is designed to avoid traveling back to a potential minimum it has visited during an energy landscape exploration. Therefore when we used

the method to generate the deformation trajectory, we tacitly assumed that back jumps could be ignored. Such an assumption is valid in this case where there are many competitive deformation paths on the trajectory and an applied driving force (i.e. mechanical stress) makes back jumps unlikely. However, in situations where highly correlated diffusion moves occur, the fact that ABC does not permit back jumps would lead to invalid rate conclusions. For such a case where the properties of the unit processes also defy the use of NEB in transition-state search, none of the approaches outlined in this thesis could be used. A situation like this is not merely hypothetical; the dislocation climb velocity problem could arguably be included in such a category. Despite the great number of calculations performed to obtain transition energies, summarized in Table 4.1, Table 4.2, and Figure 4-4, the calculated values realistically apply to only one out of 6 possible non-screw dislocation types in the system of $\frac{a}{2}\langle 111 \rangle$ dislocations on $\{110\}$ planes [71]. When one notes that this in turn is only one system out of many that may operate in the BCC structure [10], one could conclude that to calculate enough barriers to obtain a complete description of vacancy-driven dislocation climb, even with the simplifications and cutoffs mentioned in Chapter 4, is virtually impossible. However, as the driving force (i.e. stress field of the dislocation) is not sufficiently strong to prevent back jumps and as correlation effects are necessary in the description of the diffusion problem, ABC is not an appropriate solution strategy either. There is therefore much room for the continual development of new techniques and methods.

In summary, we successfully applied atomistic techniques to calculate rate and rate information for a range of long-timescale problems of microstructural evolution. These solution strategies are similar in that they are all built around the principle of understanding the rate using the atomistic transition-states, but in their implementation they all differ according to the properties of the systems. The four problems in this thesis are therefore complementary. The methods discussed in this thesis could be transferred

for use to calculate rate in other problems of slow dynamics where the characteristics of the atomic unit processes are similar. However, there are still types of problems which are not addressed within this thesis which are open to development of alternative strategies of using atomistic techniques to calculate rate.

Bibliography

[1]   J. D. Gale and A. L. Rohl, "The General Utility Lattice Program (GULP)," *Mol. Simul.*, vol. 29, pp. 291-341, 2003.

[2]   F. R. N. Nabarro, "Creep at Very Low Rates," *Metall. Mater. Trans. A*, vol. 33, p. 213, 2002.

[3]   D. Frenkel and B. Smit, *Understanding Molecular Simulation: From Algorithms to Applications.* Academic Press, San Diego, CA, 2002.

[4]   P. Vashishta, R. K. Kalia, and A. Nakano, "Multimillion Atom Molecular-Dynamics Simulations of Nanostructured Materials and Processes on Parallel Computers," in *Handbook of Materials Modeling* (S. Yip, ed.), pp. 875–928, Springer, Dordrecht, The Netherlands, 2005.

[5]   G. H. Vineyard, "Frequency Factors and Isotope Effects in Solid State Rate Processes," *J. Phys. Chem. Solids*, vol. 3, pp. 121-127, 1957.

[6]   P. G. Shewmon, *Diffusion in Solids.* Minerals, Metals & Materials Society, Warrendale, Pa., 1989.

[7]   H. Okamoto, "The C-Fe (Carbon-Iron) System," *J. Phase Equilib. Diffus.*, vol. 13, pp. 1547-7037, 1992.

[8]   C. Domain, C. S. Becquart, and J. Foct, "Ab Initio Study of Foreign Interstital Atom (C, N) Interactions with Intrinsic Point Defects in α-Fe," *Phys. Rev. B*, vol. 69, p. 144112, 2004.

[9]   C. K. Syn, D. R. Lesuer, O. D. Sherby, and E. M. Taleff, "Stress-Strain Rate Relations in Ultrahigh Carbon Steels Deformed in the Ferrite Range of Temperature," *Mater. Sci. Forum*, vol. 426-432, pp. 853-858, 2003.

[10] T. H. Courtney, *Mechanical Behavior of Materials*. McGraw-Hill, Boston, 2000.

[11] J. Weertman, "Theory of Steady-State Creep Based on Dislocation Climb," *J. Appl. Phys.*, vol. 26, pp. 1213-1217, 1955.

[12] W. D. Nix, R. Gasca-Neri, and J. P. Hirth, "A Contribution to the Theory of Dislocation Climb," *Philos. Mag.*, vol. 23, pp. 1339-1349 1971.

[13] M. F. Toney, A. J. Davenport, L. J. Oblonsky, M. P. Ryan, and C. M. Vitus, "Atomic Structure of the Passive Oxide Film Formed on Iron," *Phys. Rev. Lett.*, vol. 79, pp. 4282-4285, 1997.

[14] D. D. Macdonald, "Passivity - the Key to Our Metals-Based Civilization," *Pure Appl. Chem.*, vol. 71, pp. 951-978, 1999.

[15] S. Yip, "Nanocrystals: The Strongest Size," *Nature*, vol. 391, pp. 532-533, 1998.

[16] H. Van Swygenhoven, M. Spaczer, A. Caro, and D. Farkas, "Competing Plastic Deformation Mechanisms in Nanophase Metals," *Phys. Rev. B*, vol. 60, p. 22, 1999.

[17] V. Yamokov, D. Wolf, S. R. Phillpot, and H. Gleiter, "Grain-Boundary Diffusion Creep in Nanocrystalline Palladium by Molecular-Dynamics Simulation," *Acta Mater.*, vol. 50, pp. 61-73, 2002.

[18] J. P. Hirth and J. Lothe, *Theory of Dislocations*. McGraw-Hill Book Company,

New York, 1968.

[19] R. Dieckmann, "Defects and Cation Diffusion in Magnetite (IV): Nonstoichiometry and Point Defect Structure of Magnetite ($Fe_{3-\delta}O_4$)," *Ber. Bunsen-Ges. Phys. Chem.*, vol. 86, pp. 112-118, 1982.

[20] R. Dieckmann and H. Schmalzried, "Defects and Cation Diffusion in Magnetite (VI): Point Defect Relaxation and Correlation in Cation Tracer Diffusion," *Ber. Bunsen-Ges. Phys. Chem.*, vol. 90, pp. 564-575, 1986.

[21] J. D. Doll, "A Modern Perspective on Transition State Theory," in *Handbook of Materials Modeling* (S. Yip, ed.), pp. 1573–1583, Springer, Dordrecht, The Netherlands, 2005.

[22] R. M. Martin, *Electronic Structure: Basic Theory and Practical Methods*. Cambridge University Press, Cambridge, United Kingdom, 2004.

[23] E. Artacho, J. D. Gale, A. García, J. Junquera, R. M. Martin, P. Ordejón, D. Sánchez-Portal, and J. M. Soler, "Electronic Structure Calculations with Localized Orbitals: The SIESTA Method," in *Handbook of Materials Modeling* (S. Yip, ed.), pp. 77–91, Springer, Dordrecht, The Netherlands, 2005.

[24] G. Kresse and J. Hafner, "Ab Initio Molecular Dynamics for Liquid Metals," *Phys. Rev. B*, vol. 47, p. 558, 1993.

[25] C. J. Först, J. Slycke, K. J. Van Vliet, and S. Yip, "Point Defect Concentrations in Metstable Fe-C Alloys," *Phys. Rev. Lett.*, vol. 96, p. 177501, 2006.

[26] M. W. Finnis and J. E. Sinclair, "A Simple Empirical N-Body Potential for

Transition Metals," *Philos. Mag. A*, vol. 50, pp. 45-55, 1984.

[27] M. S. Daw and M. I. Baskes, "Embedded-Atom Method: Derivation and Application to Impurities, Surfaces, and Other Defects in Metals," *Phys. Rev. B*, vol. 29, pp. 6443-6453, 1984.

[28] G. J. Ackland, "Two-Band Second Moment Model for Transition Metals and Alloys," *J. Nucl. Mater.*, vol. 351, pp. 20-27, 2006.

[29] G. J. Ackland, M. W. Finnis, and V. Vitek, "Validity of the Second Moment Tight-Binding Model," *J. Phys. F: Met. Phys.*, vol. 18, pp. L153-L157, 1988.

[30] J. R. Shewchuk, "An Introduction to the Conjugate Gradient Method Without the Agonizing Pain," in *Technical Report, School of Computer Science*, Carnegie Mellon University, Pittsburgh, PA, 1994.

[31] A. Banerjee, N. Adams, J. Simons, and R. Shepard, "Search for Stationary Points on Surfaces," *J. Phys. Chem.*, vol. 89, pp. 52-57, 1985.

[32] M. T. Heath, *Scientific Computing, An Introductory Survey*. McGraw-Hill Science/Engineering/Math, New York, 2002.

[33] C. R. A. Catlow, "Energy Minimization Techniques in Materials Modeling," in *Handbook of Materials Modeling* (S. Yip, ed.), pp. 547–564, Springer, Dordrecht, The Netherlands, 2005.

[34] H. Jónsson, G. Mills, and K. W. Jacobsen, "Nudged Elastic Band Method for Finding Minimum Energy Paths of Transitions," in *Classical and Quantum Dynamics in Condensed Phase Simulations* (B. J. Berne, G. Ciccotti and D. F.

Coker, eds.), pp. 385-404, World Scientific Publishing Company, Hackensack, NJ, 1998.

[35] G. Henkelman, B. P. Uberuaga, and H. Jónsson, "A Climbing Image Nudged Elastic Band Method for Finding Saddle Points and Minimum Energy Paths," *J. Chem. Phys.*, vol. 113, pp. 9901-9904, 2000.

[36] G. Henkelman and H. Jónsson, "Improved Tangent Estimate in the Nudged Elastic Band Method for Finding Minimum Energy Paths and Saddle Points," *J. Chem. Phys.*, vol. 113, pp. 9978-9985, 2000.

[37] A. Kushima, X. Lin, J. Li, X. Qian, J. Eapen, J. C. Mauro, P. Diep, and S. Yip, "Computing Transition Pathways in Bulk Activated Processes: Viscosity of Supercooled Liquids," *J. Chem. Phys.*, vol. (submitted), 2008.

[38] B. P. Feuston and S. H. Garofalini, "Empirical Three-Body Potential for Vitreous Silica," *J. Chem. Phys.*, vol. 89, pp. 5818-5824, 1988.

[39] W. Kob and H. C. Andersen, "Testing Mode-Coupling Theory for a Supercooled Binary Lennard-Jones Mixture I: The van Hove Correlation Function," *Phys. Rev. E*, vol. 51, pp. 4626-4641, 1995.

[40] C. A. Angell, "Formation of Glasses from Liquids and Biopolymers," *Science*, vol. 267, pp. 1924-1935, 1995.

[41] J. Wadsworth, "The Evolution of Ultrahigh Carbon Steels - from the Great Pyramids, to Alexander the Great, to Y2K," in *Deformation, Processing, and Properties of Structural Materials: A Symposium Honoring Professor Oleg D. Sherby*, The Minerals, Metals And Materials Society, pp. 3-24, Nashville, TN,

2000.

[42] M. J. Manjoine, "Influence of Rate of Strain and Temperature on Yield Stress of Mild Steels," *J. Appl. Mech. J Appl Mech*, vol. 11, pp. A211-A218, 1944.

[43] M. J. Harrigan and O. D. Sherby, "Kinetics of Spheroidization of a Eutectoid Composition Steel as Influenced by Concurrent Straining," *Mater. Sci. Eng.*, vol. 7, pp. 177-182, 1971.

[44] J. A. Slane, C. Wolverton, and R. Gibala, "Experimental and Theoretical Evidence for Carbon-Vacancy Binding in Austenite," *Metall. Mater. Trans. A*, vol. 35, pp. 2239-2245, 2004.

[45] J. Fillon and D. Calais, "Autodiffusion dans Les Alliages Concentres fer-Palladium Self-Diffusion in Fe-Pd Alloys," *J. Phys. Chem. Solids*, vol. 38, pp. 81-89, 1977.

[46] J. W. Miller, "Diffusion of Interstitial Solute-Vacancy Pairs in a Dilute Alloy," *Phys. Rev.*, vol. 188, pp. 1074-1080, 1969.

[47] C. Domain and C. S. Becquart, "Ab Initio Calculations of Defects in Fe and Dilute Fe-Cu Alloys," *Phys. Rev. B*, vol. 65, p. 024103, 2001.

[48] W. C. Chiou and E. A. Carter, "Structure and Stability of Fe_3C-Cementite Surfaces from First Principles," *Surf. Sci.*, vol. 530, pp. 87-100, 2003.

[49] R. A. Johnson, G. J. Dienes, and A. C. Damask, "Calculations of the Energy and Migration Characteristics of Carbon and Nitrogen in α-Iron and Vanadium," *Acta Metall.*, vol. 12, pp. 1215-1224, 1964.

[50] M. Ruda, D. Farkas, and J. Abriata, "Interatomic Potentials for Carbon Interstitials

in Metals and Intermetallics," *Scr. Mater.*, vol. 46, pp. 349-355, 2002.

[51] V. Rosato, "Comparative Behavior of Carbon in BCC and FCC Iron," *Acta Metall.*, vol. 37, pp. 2759-2763, 1989.

[52] T. T. Lau, C. J. Först, X. Lin, J. D. Gale, S. Yip, and K. J. Van Vliet, "Many-Body Potential for Point Defect Clusters in Fe-C Alloys," *Phys. Rev. Lett.*, vol. 98, p. 215501, 2007.

[53] J. A. Rayne and B. S. Chandrasekhar, "Elastic Constants of Iron from 4.2 to 300°K," *Phys. Rev.*, vol. 122, pp. 1715-1716, 1961.

[54] M. Mondino and A. Seeger, "On the Interaction of Foreign Interstitial Atoms with Vacancies in α-Fe and Group-V Transition Metals," *Scr. Metall.*, vol. 11, pp. 817-823, 1977.

[55] R. A. Arndt and A. C. Damask, "Kinetics of Carbon Precipitation in Irridiated Iron. III. Calorimetry," *Acta Metall.*, vol. 12, pp. 341-345, 1964.

[56] A. Vehanen, P. Hautojärvi, J. Johansson, J. Yli-Kauppila, and P. Moser, "Vacancies and Carbon Impurities in α-Iron: Electron Irradiation," *Phys. Rev. B*, vol. 25, p. 762, 1982.

[57] D. J. Hepburn and G. J. Ackland, "Metallic-Covalent Interatomic Potential for Carbon in Iron," *Phys. Rev. B*, vol. 78, p. 165115, 2008.

[58] H.-E. Schaefer, K. Maier, M. Weller, D. Herlach, A. Seeger, and J. Diehl, "Vacancy Formation in Iron Investigated by Positron Annihilation in Thermal Equilibrium," *Scr. Metall.*, vol. 11, pp. 803-809, 1977.

[59] A. Seeger, "Lattice Vacancies in High-Purity α-Iron," *Phys. Status Solidi A*, vol. 167, pp. 289-311, 1998.

[60] C. H. Woo and W. Frank, "Void Growth and Vacancy Migration Enthalpy in Alpha-Iron," *Radiat. Eff. Defects Solids*, vol. 77, pp. 49-55, 1983.

[61] K. Tapasa, A. V. Barashev, D. J. Bacon, and Y. N. Osetsky, "Computer Simulation of Carbon Diffusion and Vacancy–Carbon Interaction in α-Iron," *Acta Mater.*, vol. 55, pp. 1-11, 2007.

[62] H. Mehrer, "Tracer Diffusion by a Divacancy Mechanism in BCC Lattices," *J. Phys. F: Met. Phys.*, vol. 3, pp. 543-547, 1973.

[63] I. V. Belova, D. S. Gentle, and G. E. Murch, "Diffusion Kinetics for Divacancies in the BCC Lattice," *Philos. Mag. Lett.*, vol. 82, pp. 37-41, 2002.

[64] D. R. Lesuer, C. K. Syn, J. D. Whittenbergerb, M. Carsic, O. A. Ruanoc, and O. D. Sherby, "Creep Behavior of Fe-C Alloys at High Temperatures and High Strain Rates," *Mater. Sci. Eng., A*, vol. 317, pp. 101-107 2001.

[65] E. Clouet, "Dislocation Interaction with C in α-Fe: A Comparison between Atomic Simulations and Elasticity Theory," *Acta Mater.*, vol. 56, pp. 3450-3460, 2008.

[66] T. T. Lau, X. Lin, S. Yip, and K. J. Van Vliet, "Atomistic Examination of the Unit Processes and Vacancy-Dislocation Interaction in Dislocation Climb," *Scr. Mater.*, vol. 60, pp. 399–402, 2009.

[67] J. P. Hirth, "Effects of Hydrogen on the Properties of Iron and Steel," *Metall. Trans. A*, vol. 11A, pp. 861-890, 1980.

[68] F. R. N. Nabarro, "Steady-State Diffusional Creep," *Philos. Mag.*, vol. 16, pp. 231-237, 1967.

[69] G. Martin and F. Soisson, "Kinetic Monte Carlo Method to Model Diffusion Controlled Phase Transformations in the Solid State," in *Handbook of Materials Modeling* (S. Yip, ed.), pp. 2223–2248, Springer, Dordrecht, The Netherlands, 2005.

[70] E. Clouet, "The Vacancy-Edge Dislocation Interaction in FCC Metals: A Comparison between Atomic Simulations and Elastic Theory," *Acta Mater.*, vol. 54, pp. 3543-3552, 2006.

[71] V. Vitek, "Theory of the Core Structures of Dislocations in Body-Centered-Cubic Metals," *Cryst. Lattice Defects*, vol. 5, pp. 1-34, 1974.

[72] S. Simonetti, M. E. Pronsato, G. Brizuela, and A. Juan, "The Electronic Effect of Carbon and Hydrogen in an (1 -1 1) Edge Dislocation Core System in BCC Iron," *Appl. Surf. Sci.*, vol. 217, pp. 56-67, 2003.

[73] W. Cai, V. V. Bulatov, J. Chang, J. Li, and S. Yip, "Periodic Image Effects in Dislocation Modeling," *Philos. Mag.*, vol. 83, pp. 539-567, 2003.

[74] J. R. K. Bigger, D. A. McInnes, A. P. Sutton, M. C. Payne, I. Stich, R. D. King-Smith, D. M. Bird, and L. J. Clarke, "Atomic and Electronic Structures of the 90° Partial Dislocation in Silicon," *Phys. Rev. Lett.*, vol. 69, pp. 2224-2227 1992.

[75] M. Yamaguchi and V. Vitek, "Core Structure of Nonscrew 1/2 <111> Dislocations on {110} Planes in BCC Crystals I. Core Structure in an Unstressed Crystal," *J. Phys. F: Met. Phys.*, vol. 3, pp. 523-536, 1973.

[76] V. Vitek and M. Yamaguchi, "Core Structure of Nonscrew 1/2 <111> Dislocations on {110} Planes in BCC Crystals II. Peierls Stress and the Effect of an External Shear Stress on the Cores," *J. Phys. F: Met. Phys.*, vol. 3, pp. 537-542, 1973.

[77] W. Cai, *Atomistic and Mesoscale Modeling of Dislocation Mobility*. Ph.D. thesis, Massachusetts Institute of Technology, 2001.

[78] J. Li, "AtomEye: an Efficient Atomistic Configuration Viewer," *Modelling Simul. Mater. Sci. Eng.*, vol. 11, pp. 173-177, 2003.

[79] Y. Kamimura, T. Tsutsumi, and E. Kuramoto, "Calculations of Positron Lifetimes in a Jog and Vacancies on an Edge-Dislocation Line in Fe," *Phys. Rev. B*, vol. 52, pp. 879-885, 1995.

[80] A. N. Stroh, "Dislocations and Cracks in Anisotropic Elasticity," *Philos. Mag.*, vol. 3, p. 265, 1958.

[81] A. B. Bortz, M. H. Kalos, and J. L. Lebowitz, "A New Algorithm for Monte Carlo Simulation of Ising Spin Systems," *J. Comput. Phys.*, vol. 17, pp. 10-18, 1975.

[82] D. Mordehai, E. Clouet, M. Fivel, and M. Verdier, "Introducing Dislocation Climb by Bulk Diffusion in Discrete Dislocation Dynamics," *Philos. Mag.*, vol. 88, pp. 899–925, 2008.

[83] A. J. Davenport, L. J. Oblonsky, M. P. Ryan, and M. F. Toney, "The Structure of the Passive Film That Forms on Iron in Aqueous Environments," *J. Electrochem. Soc.*, vol. 147, pp. 2162-2173, 2000.

[84] M. S. Odziemkowski, T. T. Schuhmacher, and R. W. R. Gillham, E.J., "Mechanism

of Oxide Film Formation on Iron in Simulating Groundwater Solutions: Raman Spectroscopic Studies," *Corros. Sci.*, vol. 40, pp. 371-389, 1998.

[85] S. C. Hendy, B. Walker, N. J. Laycock, and M. P. Ryan, "Ab Initio Studies of the Passive Film Formed on Iron," *Phys. Rev. B*, vol. 67, p. 085407, 2003.

[86] N. L. Peterson, W. K. Chen, and D. Wolf, "Correlation and Isotope Effects for Cation Diffusion in Magnetite," *J. Phys. Chem. Solids*, vol. 41, pp. 709-719, 1980.

[87] G. B. Barbi, "Thermodynamic Functions and Phase Stability Limits by Electromotive Force Measurements on Solid Electrolytic Cells," *J. Phys. Chem.*, vol. 68, pp. 1025–1029, 1964.

[88] H. Rau, "Thermodynamics of the Reduction of Iron Oxide Powders with Hydrogen," *J. Chem. Thermodyn.*, vol. 4, pp. 57-64, 1972.

[89] R. Dieckmann, "Point Defects and Transport in Non-Stoichiometric Oxides: Solved and Unsolved Problem," *J. Phys. Chem. Solids*, vol. 59, pp. 507-525, 1998.

[90] Z. Zhang and S. Satpathy, "Electron States, Magnetism, and the Verwey Transition in Magnetite," *Phys. Rev. B*, vol. 44, pp. 13319-13331 1991.

[91] V. I. Anisimov, I. S. Elfimov, N. Hamada, and K. Terakura, "Charge-Ordered Insulating State of Fe_3O_4 from First-Principles Electronic Structure Calculations," *Phys. Rev. B*, vol. 54, pp. 4387-4390, 1996.

[92] L. Wang, T. Maxisch, and G. Ceder, "Oxidation Energies of Transition Metal Oxides within the GGA+U Framework," *Phys. Rev. B*, vol. 73, p. 195107, 2006.

[93] G. Grosso and G. Pastori Parravicini, *Solid State Physics*. Academic Press, San Diego, California, 2000.

[94] S. L. Dudarev, G. A. Botton, S. Y. Savrasov, C. J. Humphreys, and A. P. Sutton, "Electron-Energy-Loss Spectra and the Structural Stability of Nickel Oxide: An LSDA+U Study," *Phys. Rev. B*, vol. 57, pp. 1505-1509, 1998.

[95] S. C. Hendy, N. J. Laycock, and M. P. Ryan, "Atomistic Modeling of Cation Transport in the Passive Film on Iron and Implications for Models of Growth Kinetics," *J. Electrochem. Soc.*, vol. 152, pp. B271-B276, 2005.

[96] G. V. Lewis, C. R. A. Catlow, and A. N. Cormack, "Defect Structure and Migration in Fe_3O_4," *J. Phys. Chem. Solids*, vol. 46, pp. 1227-1233, 1985.

[97] J. M. Daniels and A. Rosencwaig, "Mössbauer Spectroscopy of Stoichiometric and Non-Stoichiometric Magnetite," *J. Phys. Chem. Solids*, vol. 30, pp. 1561-1571, 1969.

[98] T. Langdon, "Grain Boundary Sliding Revisited: Developments in Sliding over Four Decades," *J. Mater. Sci.*, vol. 41, pp. 597-609, 2006.

[99] W. A. Rachinger, "Relative Grain Translations in the Plastic Flow of Aluminium," *J. Inst. Metals*, vol. 81, pp. 33-41, 1952.

[100] I. M. Lifshitz, "On the Theory of Diffusion-Viscous Flow of Polycrystalline Bodies," *Zh. Eksp. Teor. Fiz.*, vol. 44, pp. 1349–1367, 1963.

[101] A. K. Mukherjee, "Rate Controlling Mechanism in Superplasticity," *Mater. Sci. Eng.*, vol. 8, pp. 83-89, 1971.

110

[102] J. Schiøtz, T. Vegge, F. D. Di Tolla, and K. W. Jacobsen, "Atomic-Scale Simulations of the Mechanical Deformation of Nanocrystalline Metals," *Phys. Rev. B*, vol. 60, pp. 11971-11983, 1999.

[103] J. P. Hirth, "Dislocations, Steps and Disconnections at Interfaces," *J. Phys. Chem. Solids*, vol. 55, pp. 985-989, 1994.

[104] S. Namilae, N. Chandra, and T. G. Nieh, "Atomistic Simulation of Grain Boundary Sliding in Pure and Magnesium Doped Aluminum Bicrystal," *Scr. Mater.*, vol. 46, pp. 49-54, 2002.

[105] R. J. Kurtz, R. G. Hoagland, and J. P. Hirth, "Effect of Extrinsic Grain-Boundary Defects on Grain-Boundary Sliding Resistance," *Philos. Mag. A*, vol. 79, pp. 665-681, 1999.

[106] P. Keblinski, D. Wolf, S. R. Phillpot, and H. Gleiter, "Self-Diffusion in High-Angle FCC Metal Grain Boundaries by Molecular Dynamics Simulation," *Philos. Mag. A*, vol. 79, pp. 2735-2761, 1999.

[107] E. Bonetti, E. G. Campari, L. Del Bianco, L. Pasquini, and E. Sampaolesi, "Mechanical Behaviour of Nanocrystalline Iron and Nickel in the Quasi-Static and Low Frequency Anelastic Regime," *NanoStructured Materials*, vol. 13, pp. 709-720, 1999.

[108] A. Kokalj, "Computer Graphics and Graphical User Interfaces as Tools in Simulations of Matter at the Atomic Scale," *Comput. Mater. Sci.*, vol. 28, pp. 155-168, 2003.

About the Author

Mr. Timothy Lau was born in Hong Kong in 1984. He graduated *summa cum laude*, with honors, from Cornell University in 2005 in the area of Materials Science and Engineering. He joined the Department of Materials Science and Engineering of the Massachusetts Institute of Technology in 2005 and started his Ph.D. thesis research on atomistic calculations of rate with Professor Sidney Yip. Mr. Lau has been awarded the National Defense Science and Engineering Graduate (NDSEG) Fellowship in 2005 and the National Science Foundation Graduate Research Fellowship Program (NSFGFRP) Honorable Mention in 2005 and in 2006. He is a member of Tau Beta Pi and Sigma Xi. He will pursue a career in law.